

Topological flowscape reveals state transitions in nonreciprocal living matter

Hyunseok Lee^{1,6}, EliseAnne Koskelo^{1,2,6}, Shreyas Gokhale^{1,6}, Junang Li^{3,6}, Chenyi Fei⁴, Chih-Wei Joshua Liu¹, Lisa Lin¹, Jörn Dunkel⁴, Dominic J Skinner⁵, and Nikta Fakhri^{1*}

¹ Department of Physics, Massachusetts Institute of Technology, Cambridge, MA, USA

² Department of Physics, Harvard University, Cambridge, MA, USA

³ Center for the Physics of Biological Function, Princeton University, Princeton, NJ, USA

⁴ Department of Mathematics, Massachusetts Institute of Technology, Cambridge, MA, USA

⁵ Center for Computational Biology, Flatiron Institute, New York, NY, USA

⁶ These authors contributed equally and are joint first authors.

(Dated: November 20, 2025)

Nonreciprocal interactions—where forces between entities are asymmetric—govern a wide range of nonequilibrium phenomena, yet their role in structural transitions in living and active systems remains elusive. Here, we demonstrate a transition between nonreciprocal states using starfish embryos at different stages of development, where interactions are inherently asymmetric and tunable. Experiments, interaction inference, and topological analysis yield a nonreciprocal state diagram spanning crystalline, flocking, and fragmented states, revealing that weak nonreciprocity promotes structural order while stronger asymmetry disrupts it. To capture these transitions, we introduce topological landscapes, mapping the distribution of structural motifs across state space. We further develop topological flowscapes, a dynamic framework that quantifies transitions between collective states and detects an informational rate shift from the experimental state transition. Together, these results establish a general approach for decoding nonequilibrium transitions and uncover how asymmetric interactions sculpt the dynamical and structural architecture of active and living matter.

Nature produces diverse structures and behaviors whose complexity greatly surpasses equilibrium constraints [1, 2]. From flocks of birds [3, 4] and colonies of microbes [5–9] to cellular tissues [10, 11] and synthetic active materials [12, 13], remarkable forms and functionalities emerge spontaneously from local interactions among constituents, without external coordination. This self-organized emergence, driven by the agency of individual components, not only underpins biological complexity but also inspires new classes of active and adaptive materials, where nonequilibrium dynamics are harnessed for novel functionalities [14–19].

At the core of these complex phenomena lie nonreciprocal interactions, where action and reaction between components are inherently asymmetric [19–23]. Such asymmetry profoundly influences nonequilibrium behavior, driving rich dynamical phenomena including traveling waves [21, 22, 24, 25], spontaneous oscillations [23, 26, 27], and chiral flows [28]. Yet, despite growing recognition of their significance, how nonreciprocity shapes structural transitions and the emergence of stable configurations remains largely unexplored [29–34]. Furthermore, the extent to which nonreciprocity governs information transfer and state evolution in living systems is unclear [35, 36].

Here, we address this gap by investigating how nonreciprocity orchestrates collective self-organization and structural transitions in a biologically tunable system:

starfish embryos at distinct developmental stages, which interact through inherently asymmetric fluid-mediated forces. Building upon our previous discovery of living chiral crystals composed of homogeneous embryo ensembles [37], we systematically examine binary mixtures of embryos at different developmental ages. Through experiments integrated with interaction inference and novel topological analyses, we identify distinct emergent states, including crystalline, self-propelled crystalline, flocking, and fragmented configurations. We introduce topological landscapes, revealing symmetry-breaking transitions between these nonreciprocal states, and topological flowscapes, quantifying the informational trajectory of the transitions. These conceptual tools provide a versatile framework to uncover structural and dynamic transitions across biological and synthetic active matter.

A NONRECIPROCAL MIXTURE OF STARFISH EMBRYOS TRANSITIONS FROM A TRAVELING STATE TO A FLUCTUATING STATE

To experimentally uncover how nonreciprocity shapes collective dynamics, we developed a living nonreciprocal system composed of embryos from the starfish *Patiria miniata*. Unlike homogeneous embryo populations, which display emergent nonreciprocity through broken chiral symmetries [37, 38], our heterogeneous system exhibits a longitudinal nonreciprocity between two types of embryos (E1 and E2), controlled by their developmental ages (Fig. 1a). Quantitative video microscopy reveals a striking run-and-chase dynamic: younger E1 embryos actively pursue older E2 embryos, whereas E2

* Corresponding author: fakhri@mit.edu

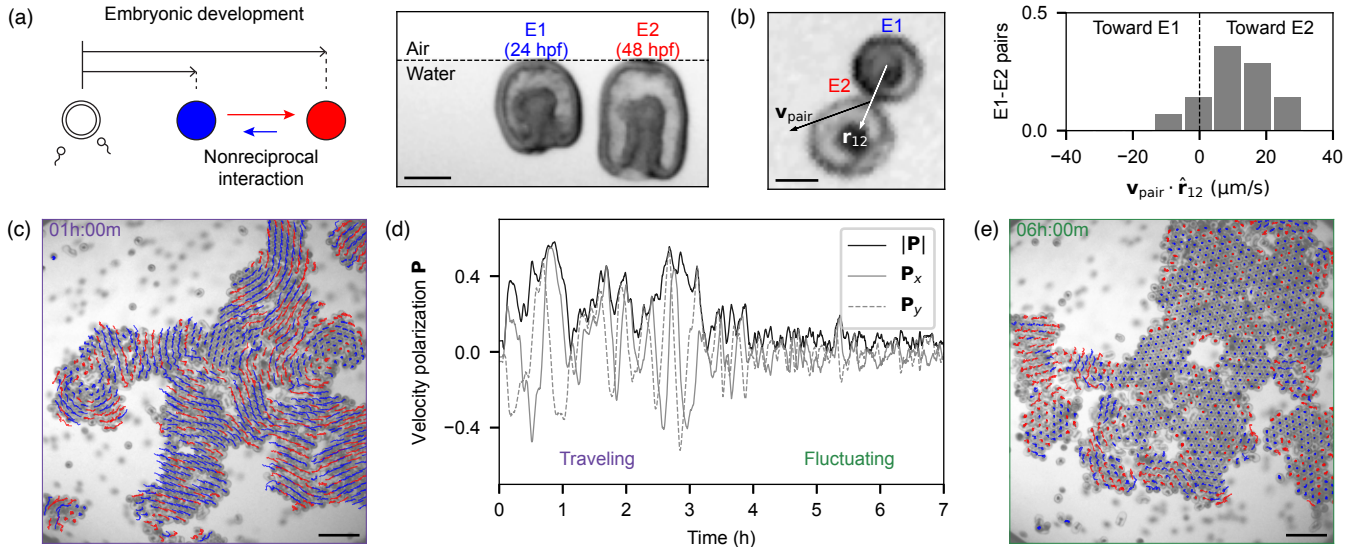


FIG. 1. A nonreciprocal mixture of starfish embryos transitions from a traveling state to a fluctuating state. (a) Nonreciprocity arises from a developmental gap between embryos. An E1 embryo (24 hours post-fertilization) and an E2 embryo (48 hours post-fertilization) form a bound pair at the air-water interface. Scale bar: 100 μm . (b) The velocity of the embryo pair, \mathbf{v}_{pair} , tends to align with the displacement vector \mathbf{r}_{12} from E1 to E2. The average drift speed toward E2, $\mathbf{v}_{\text{pair}} \cdot \hat{\mathbf{r}}_{12}$, is $12 \pm 3 \mu\text{m/s}$ (SEM, $n = 14$). Scale bar: 100 μm . (c) Snapshot of an E1-E2 mixture at 1 hour, overlaid with 2-minute trajectories (blue: E1, red: E2). Scale bar: 1 mm. (d) Time series of velocity polarization, $\mathbf{P}(t) \equiv \langle \hat{\mathbf{v}}_i(t) \rangle_i$, reveals a transition from a traveling state to a fluctuating state. Oscillations and a phase shift between \mathbf{P}_x and \mathbf{P}_y highlight the chirality of the velocity polarization, which rotates clockwise during the traveling state. (e) Snapshot of the same mixture at 6 hours, overlaid with 2-minute trajectories (blue: E1, red: E2). Scale bar: 1 mm.

embryos move preferentially away from E1 (Fig. 1b). Further experiments demonstrate that this nonreciprocal interaction arises from asymmetric precession of the embryos' anterior-posterior (AP) axes, establishing a clear physical mechanism underlying nonreciprocity (Supplementary Section I.B.3).

When thousands of E1 and E2 embryos are mixed, the system spontaneously exhibits collective translation, a hallmark of nonreciprocal interactions [22]. Initially, the embryos flock together, forming a dynamically ordered *traveling* state characterized by strong polar alignment, quantified by the velocity polarization order parameter $\mathbf{P} \equiv \langle \hat{\mathbf{v}}_i \rangle_i$ (Fig. 1c-d). Remarkably, this polar order emerges exclusively in mixed-age embryo populations, whereas it is absent in homogeneous populations, thus experimentally verifying the theoretical prediction that nonreciprocity is essential for emergent polar order [21, 22]. The velocity polarization \mathbf{P} is time-dependent, rotating clockwise with a fluctuating magnitude (Fig. 1d and Supplementary Section I.C.3). This rotation arises from broken chiral symmetry of individual embryos rather than from emergent chirality via nonreciprocal alignment [23]. Furthermore, we find that E2 embryos consistently lead E1 in collective translation, confirming that nonreciprocity drives the flocking of embryos (Supplementary Section I.C.4).

After hours of collective translation, the embryo mix-

ture transitions into a distinct self-organized state. In this *fluctuating* state, embryos arrange into an ordered lattice, while small fluctuations arise from self-generated hydrodynamic flows (Fig. 1e and Supplementary Section I.C.5). As a result, the velocity polarization \mathbf{P} exhibits near-zero fluctuations, demarcating the departure from the traveling state (Fig. 1d). The transition from ordered dynamics to ordered configurations reveals a rich state space of nonequilibrium behaviors that depend on nonreciprocity. By tuning nonreciprocity, the system exhibits a wide variety of emergent collective states, including chiral orbits and demixed regimes. This tunability highlights the versatility of the experimental platform (Supplementary Section I.D).

TOPOLOGICAL METRIC DISTINGUISHES EMERGENT STATES IN AN INFERENCE-BASED MODEL OF NONRECIPROCAL MIXTURES

To systematically map the nonequilibrium states of nonreciprocal mixtures, we tune the inter-type longitudinal nonreciprocity \mathcal{N} in a pairwise interaction model. The underlying interactions are extracted from many-body experimental trajectories using a data-driven inference that reconstructs the most likely longitudinal and transverse forces between embryo pairs as functions of their separation and types (E1 or

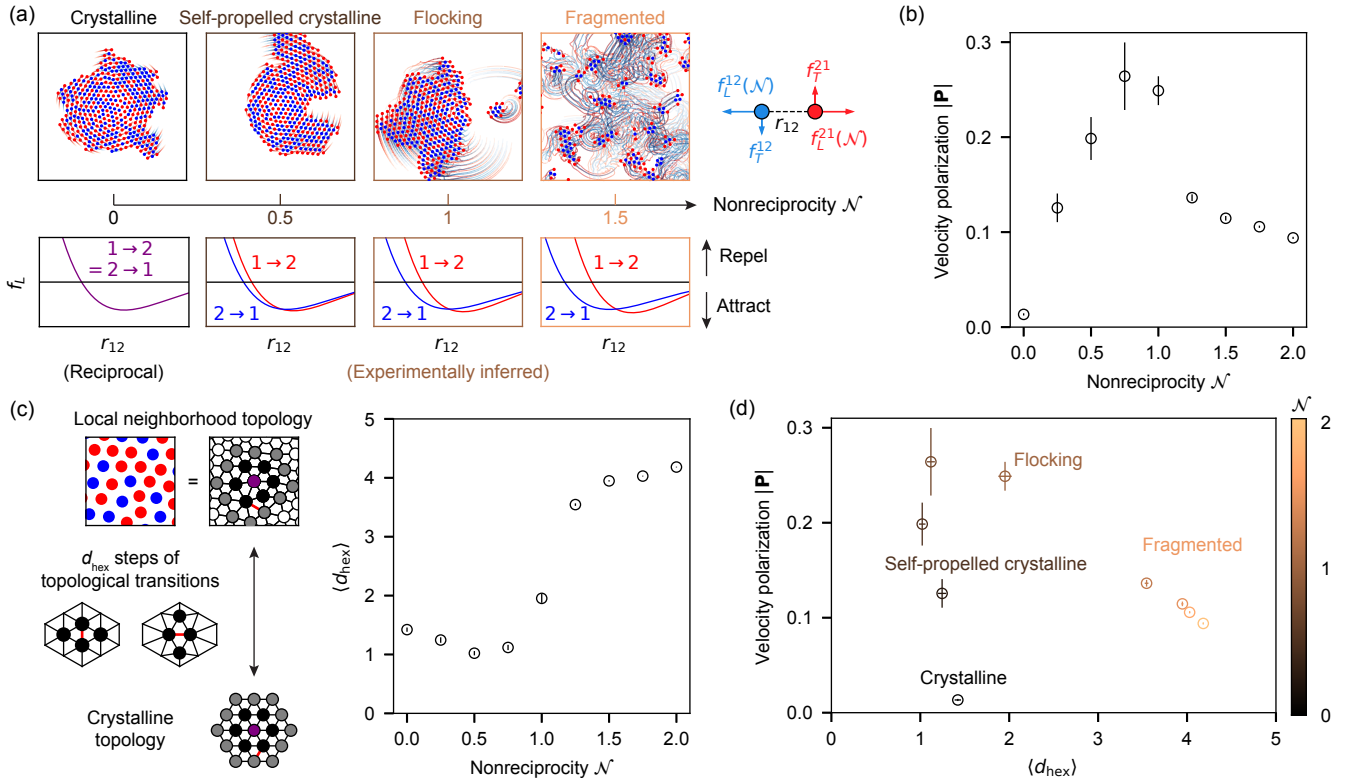


FIG. 2. **Topological order parameter distinguishes emergent states in an inference-based model of nonreciprocal mixtures.** (a) In the inference-based model, we use experimentally inferred pairwise interactions $f_{L/T}^{ij}$, except for longitudinal inter-type interactions whose nonreciprocity is scaled by \mathcal{N} . The model exhibits four distinct states as the nonreciprocity \mathcal{N} increases: crystalline, self-propelled crystalline, flocking, and fragmented states. (b) Velocity polarization magnitude $|\mathbf{P}|$ as a function of \mathcal{N} , averaged over 20 initial configurations (error bars: SEM). $|\mathbf{P}|$ decreases for $\mathcal{N} > 1$. (c) *Left:* The structural metric d_{hex} quantifies the number of local topological (T1) transitions relative to a perfect hexagonal crystal; red edges highlight topology-changing transitions. *Right:* The structural order parameter $\langle d_{\text{hex}} \rangle$ reaches a minimum at $\mathcal{N} = 0.5$ and rises sharply at $\mathcal{N} = 1$ (error bars: SEM, $n=20$). (d) State diagram of nonreciprocal mixtures, summarizing emergent states across the pairwise nonreciprocity \mathcal{N} .

E2) [39, 40] (Supplementary Section II). Applied to the full experimental dataset, this inference yields an E1-E2 longitudinal interaction whose nonreciprocity matches the isolated run-and-chase dynamics (Fig. 1b). We take this inferred inter-type longitudinal interaction as a baseline $\mathcal{N} = 1$ and tune the interaction by scaling its asymmetric component by \mathcal{N} (Fig. 2a, Supplementary Section III). At $\mathcal{N} = 0$ (reciprocal interactions), we find a *crystalline* state that rotates clockwise, recapitulating homogeneous embryos forming living chiral crystals [37]. For $0 < \mathcal{N} < 1$ (weak nonreciprocity), we observe a *self-propelled crystalline* state, where a crystal undergoes collective translation. At $\mathcal{N} = 1$ (nonreciprocity inferred from experiment), the system exhibits *flocking*, maintaining collective motion but not a global crystalline arrangement. Instead, the crystals repeatedly merge and fragment, reflecting the early dynamics observed in embryo mixture experiments (Fig. 1d and Supplementary Section III.C). For $\mathcal{N} > 1$ (strong nonreciprocity), the system is further *fragmented*, with each fragment propelling itself in different directions.

Although existing theories of nonreciprocal interactions predict a jump in velocity polarization $|\mathbf{P}|$ as the system enters a traveling state [22, 23], our model reveals a richer complexity (Fig. 2b). The broken chiral symmetry in transverse interactions causes clusters to rotate rather than move in a straight line, competing with collective translation induced by nonreciprocity. This interplay leads $|\mathbf{P}|$ to rise continuously, rather than abruptly, with increasing \mathcal{N} . Surprisingly, we find that $|\mathbf{P}|$ peaks near $\mathcal{N} = 1$ and then decreases for $\mathcal{N} > 1$, a behavior explained by fragmentation into independently moving clusters whose internal self-propulsion dominates interactions between clusters. Consequently, states with disparate collective dynamics, such as self-propelled crystals and fragmented clusters, exhibit similar velocity polarization magnitudes despite their distinct differences in structure.

To robustly distinguish these structurally diverse states beyond velocity polarization $|\mathbf{P}|$ alone, we need a

structural order parameter. Notably, while nonreciprocity can drive structures far away from translational or orientational order, these complex arrangements can still be systematically compared through their topologies [4, 41]. Hence, we define a topological metric d_{hex} based on a recently developed topological packing statistics framework [41, 42]. This metric quantifies structural order by counting the number of local T1 topological rearrangements required to reach a perfect crystalline arrangement from a given local neighborhood (Fig. 2c and Supplementary Section IV). Accordingly, the system-average $\langle d_{\text{hex}} \rangle$ serves as a measure of the topological distance between the system's self-organized structure and a perfect crystal.

The structural order parameter $\langle d_{\text{hex}} \rangle$, which quantifies the average topological distance from a crystal, exhibits a sharp transition at nonreciprocity $\mathcal{N} = 1$ (Fig. 2c). At $\mathcal{N} < 1$, $\langle d_{\text{hex}} \rangle$ is small, indicating crystalline structures. Interestingly, we observe nonreciprocal self-healing where a weak nonreciprocity decreases $\langle d_{\text{hex}} \rangle$; topological motifs with defects, which are unstable under nonreciprocity-driven stress, are annealed into a crystalline motif which remains stable (Supplementary Section IV.D). Nevertheless, the crystalline motif eventually becomes unstable under a sufficiently strong nonreciprocity, such as the experimentally inferred $\mathcal{N} = 1$. This destabilization is captured by a sharp jump in $\langle d_{\text{hex}} \rangle$ as an annealed crystal transitions into a dynamic, multi-cluster structure.

Combining the two order parameters, $|\mathbf{P}|$ for dynamics and $\langle d_{\text{hex}} \rangle$ for structure, we construct a state diagram that maps all emergent nonreciprocal states (Fig. 2d). As nonreciprocity increases from $\mathcal{N} = 0$, $\langle d_{\text{hex}} \rangle$ decreases and $|\mathbf{P}|$ increases. Once nonreciprocity reaches the experimental $\mathcal{N} = 1$, $\langle d_{\text{hex}} \rangle$ jumps while $|\mathbf{P}|$ remains large. Finally, for $\mathcal{N} > 1$, $\langle d_{\text{hex}} \rangle$ is large while $|\mathbf{P}|$ is small. Overall, our state diagram captures nonreciprocity-driven transitions in both collective translation, which peaks at intermediate nonreciprocity, and self-organized crystalline structure, which is enhanced by weak nonreciprocity and destabilized by strong nonreciprocity.

TOPOLOGICAL LANDSCAPE ELUCIDATES A NONRECIPROCAL TRANSITION IN SELF-ORGANIZED STRUCTURE

Using the structural order parameter $\langle d_{\text{hex}} \rangle$, we observe that weak nonreciprocity stabilizes crystalline structures, whereas strong nonreciprocity leads to structural destabilization. However, this average measure does not provide insight into the precise local structural changes driving these transitions. To address this limitation, we introduce a novel approach to systematically characterize the distribution of local topologies observed in our experiments and simulations, involving approxi-

mately 15,000 distinct motifs (Supplementary Section V).

We use pairwise topological distances (defined by the number of T1 transitions) among all motifs to construct a low-dimensional manifold (Fig. 3a). This manifold positions motifs which differ by only a few T1 transitions close to each other, allowing an intuitive representation of structural proximity. Mapping motif frequencies onto this manifold as height values creates *topological landscapes*, which provide a comprehensive visualization of how local structural motifs distribute and evolve as nonreciprocity \mathcal{N} varies.

As nonreciprocity increases, these landscapes exhibit a clear transition from single-peaked to multi-peaked distributions, indicating increased structural diversity (Fig. 3b). Specifically, motif probabilities shift systematically towards a region of the manifold associated with less crystalline order. This trend aligns with the observed increase in the structural order parameter $\langle d_{\text{hex}} \rangle$, supporting the association between this manifold region and low-symmetry structures.

Further analysis identifies the atlas of frequent motifs at the experimentally inferred nonreciprocity level $\mathcal{N} = 1$ (Fig. 3c). Among those, the two dominant motifs contribute to the two peaks of the landscape: motif M_1 , corresponding to a perfect crystalline structure, and motif M_2 , representing an almost-crystalline structure with a single five-fold defect (Supplementary Section V.D). Crucially, nonreciprocity not only breaks the sixfold symmetry inherent to the perfect crystal but also introduces directional anisotropy within the motif space, selecting a preferred structural transition pathway along the M_1 – M_2 axis.

To quantitatively capture this symmetry-breaking transition, we examine one-dimensional slices of the topological landscape along the M_1 – M_2 axis (Fig. 3d). The negative log-likelihood ratio $-\log(p/p_{M_1})$ clearly reveals a global minimum at motif M_1 for low nonreciprocity levels, which deepens as \mathcal{N} increases, indicating enhanced stability of crystalline order through nonreciprocal self-healing. A second minimum emerges at motif M_2 as \mathcal{N} approaches 1, resulting in a coexistence at $\mathcal{N} = 1$ and a subsequent dominance of defect-containing motifs at higher nonreciprocity levels. This behavior is reminiscent of a first-order phase transition, offering a conceptual analogy for understanding nonequilibrium structural transitions (Supplementary Section V.E).

Extending this analysis to experimental data, we construct time-resolved experimental topological landscapes by tracking motif frequencies within temporal windows (Fig. 4a). These experimental landscapes strikingly resemble the model predictions at $\mathcal{N} = 1$, displaying identical dual-peaked distributions around motifs M_1 and M_2 . Additionally, the experimental progression over time

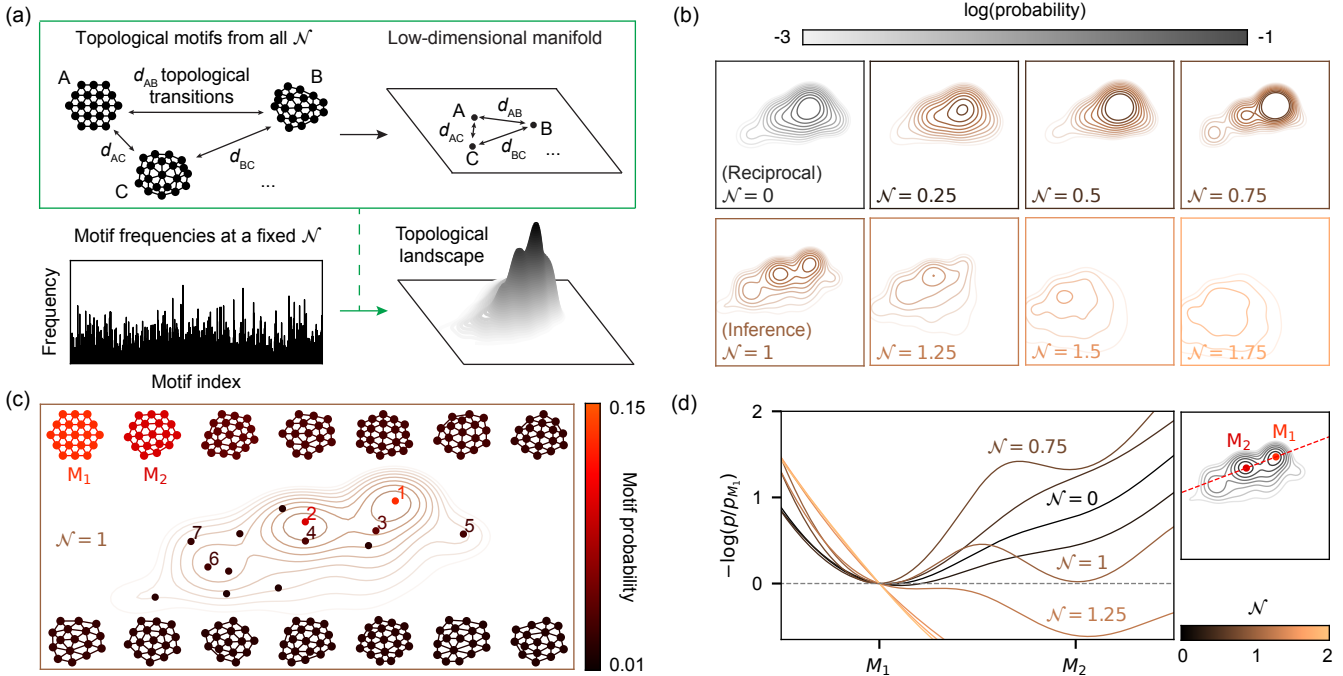


FIG. 3. Topological landscape reveals a symmetry-breaking transition in self-organized structures as nonreciprocity increases. (a) We construct a low-dimensional manifold of topological motifs based on their pairwise topological distances. The resulting *topological landscape* visualizes the probability distribution of local topologies (from each level of nonreciprocity \mathcal{N}) on this manifold. (b) Contour plots of topological landscapes display a transition from single-peaked to multi-peaked distributions as \mathcal{N} increases. (c) At $\mathcal{N} = 1$ (experimentally inferred nonreciprocity), 14 topological motifs exhibit a frequency greater than 1%. In particular, the top two dominant motifs correspond to the two distinct peaks of the topological landscape. *Top:* Motifs from M_1 to M_7 . M_1 is a perfect crystal, while M_2 contains a 5-defect. *Bottom:* Motifs from M_8 to M_{14} . See Supplementary Section V.C for an enlarged motif atlas with full annotations. (d) Negative log-likelihood ratio relative to M_1 , measured along the M_1 - M_2 axis. At $\mathcal{N} = 0$, the system shows a single minimum at M_1 . Near $\mathcal{N} = 1$, the structures undergo a first-order-like transition from M_1 -dominated to M_2 -dominated states, with coexistence at $\mathcal{N} = 1$.

mirrors the model predictions under decreasing nonreciprocity (Fig. 4b), including passage through a coexistence regime at the onset of the transition from traveling to fluctuating states, as quantified by velocity polarization dynamics. Bayesian inference confirms that pairwise nonreciprocity between embryos decreases by approximately 30% during the course of the experiment, supporting a striking correspondence between time-driven transitions in the experiment and those induced by varying nonreciprocity in the theoretical model (Supplementary Section II.B).

TOPOLOGICAL FLOWSCAPE QUANTIFIES THE TIME EVOLUTION OF TOPOLOGICAL LANDSCAPES IN THE EXPERIMENT

Topological landscapes describe steady states without explicitly capturing the dynamic pathways connecting these states. To address this limitation, we introduce the *topological flowscape*, a quantitative framework that assigns coordinates to entire landscapes, analogous to how individual topological motifs are embedded (Fig. 4c).

The coordinates for the flowscape are defined by Kullback–Leibler (KL) divergences from two informed choices of reference distributions, representing M_1 and M_2 respectively (Supplementary Section VI). These divergences quantify the distinguishability between observed system states and reference states based on local motif frequencies, providing an information-theoretic interpretation: each axis measures the informational “cost” of describing the entire system state in terms of M_1 or M_2 . Thus, the flowscape, a low-dimensional projection of the landscapes, visually captures their temporal evolution as a continuous trajectory or “flow.”

The topological flowscape quantitatively shows that the observed transition from an M_2 -dominated (disordered) state toward an M_1 -dominated (ordered) state is not gradual. Instead, around 3 hours, the system undergoes a sharp directional change, initially moving rapidly toward both motifs to subsequently drifting slowly toward M_1 while moving away from M_2 . Moreover, while the model predicts that the intermediate states are more crystalline than the final state, the experimental path deviates from this behav-

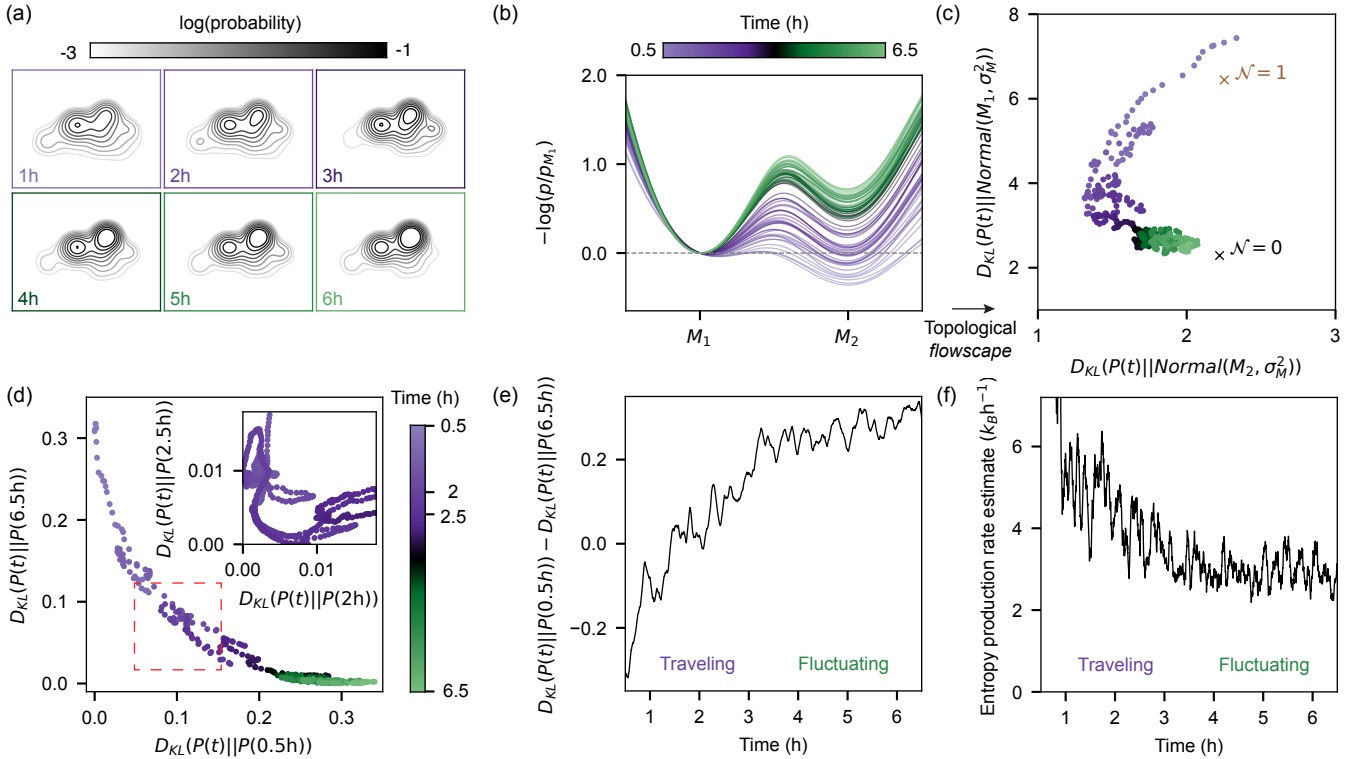


FIG. 4. Topological flowscape characterizes the time evolution of topological landscapes in the experiment. (a) Contour plots of experimental topological landscapes reveal a shifting balance between two dominant peaks over time. These peaks correspond to motifs M_1 and M_2 , previously identified in the model at the experimentally inferred nonreciprocity $\mathcal{N} = 1$. (b) Negative log-likelihood relative to M_1 , measured along the M_1 – M_2 axis. The self-organized structures transition from an M_2 -dominated to an M_1 -dominated state as the embryo mixture shifts from a traveling to a fluctuating state (Fig. 1d). (c) *Topological flowscape* of the experiment. Each landscape is mapped to a point using KL divergence from two synthetic reference distributions centered at M_1 and M_2 , with widths σ_M matched to the kernel of experimental landscape (Supplementary Section VI.B). The trajectory flows from a region near $\mathcal{N} = 1$ toward one resembling $\mathcal{N} = 0$. (d) Flowscape constructed using experimental states at different times as dynamic references. Using 0.5 h and 6.5 h as references captures a long-timescale transition. *Inset:* Using 2 h and 2.5 h as references reveals short-timescale cyclic transitions associated with cluster merging and breaking (Supplementary Section VI.E). (e) Diagonal displacement in the flowscape quantifies the log-likelihood difference between reference states. The progress is rapid during the traveling state and slows significantly in the fluctuating state. (f) Entropy production rate (EPR), estimated from changes in topological motif frequencies using thermodynamic speed limits, exhibits a similar transition as in (e), with higher rates during the traveling state and reduced rates in the fluctuating state.

ior (Supplementary Sections VI.C–D). This discrepancy indicates potential higher-order mechanisms beyond the development-driven decrease in nonreciprocity (Supplementary Section II.B), highlighting the flowscape’s potential as a tool for dissecting complex experimental dynamics.

The flexibility of reference distributions in the flowscape framework further allows us to probe structural dynamics across multiple temporal scales (Fig. 4d). Large temporal gaps between references elucidate global structural transitions, while shorter intervals reveal rapid cyclic dynamics such as repeated cluster merging and fragmentations (Supplementary Section VI.E). Furthermore, diagonal displacement in the flowscape provides a log-likelihood-based “progress bar” (Fig. 4e), tracking how the system transitions from initial to final

states. Interestingly, this displacement shows a clear rate transition that coincides with the independently measured shift in velocity polarization $|\mathbf{P}|$ from traveling to fluctuating states (Fig. 1d). This underlines a thermodynamic connection between macroscopic state transitions and microscopic structural changes.

To independently validate this rate transition, we estimate the entropy production rate (EPR) using motif transition statistics and thermodynamic speed-limit principles (Fig. 4f and Supplementary Section VII.A). The EPR independently confirms a transition from high dissipation during the traveling state to lower dissipation in the fluctuating state, mirroring the rate transition captured by the flowscape. Moreover, the information length derived from information geometry also reveals this rate shift at the state transition (Supple-

mentary Section VII.B). Together, these observations provide an experimental signature of the interplay between information-theoretic quantities and order parameters during nonequilibrium state transitions.

DISCUSSION

We have investigated the intricate self-organization and state transitions driven by nonreciprocal interactions in active living matter. Through experiments on heterogeneous populations of starfish embryos—whose developmental ages control their nonreciprocal interactions—we uncover two strikingly different nonequilibrium states: a traveling state characterized by dynamic flocking clusters, and a fluctuating state defined by a crystal-like structure and reduced displacement. By developing a predictive model, we systematically map out the broader spectrum of states, revealing that collective motion peaks at intermediate levels of nonreciprocity, while higher nonreciprocity induces structural instability and fragmentation.

To rigorously characterize these emergent states and their transitions, we introduced two novel conceptual frameworks: *topological landscapes* and *topological flowscapes*. Topological landscapes provide a powerful quantitative method for capturing local structural distributions and symmetry-breaking phenomena. Building upon this, topological flowscapes map the dynamic evolution of landscapes, quantitatively visualizing the pathway systems take through high-dimensional state spaces and pinpointing precise transitions at the intersection of microscopic structure and macroscopic order. Notably, we discovered a clear thermodynamic signature of these transitions, as evidenced by rate shifts in state evolution and entropy production.

Our conceptual framework, anchored in the notions of topological landscapes and flowscapes, offers a novel perspective for interpreting nonequilibrium systems as evolving probability landscapes. This approach is broadly applicable in diverse contexts, from synthetic active matter such as colloidal assemblies and artificial intelligence models, to complex biological processes such as neural network dynamics and multicellular devel-

opment. These tools not only elucidate the intricate dynamics observed in the experiments but can also integrate with theoretical models, presenting a unified method to analyze state transitions and emergent phenomena. More broadly, the complex temporal behaviors characteristic of nonequilibrium systems may reflect deeper underlying principles governing informational flow and organizational dynamics. By explicitly linking organization to information theory and thermodynamics, our work takes a step toward a unified framework for understanding nonequilibrium phenomena through the lens of informational dynamics.

ACKNOWLEDGMENTS

We thank Mehran Kardar for valuable discussions. This research was supported by an Alfred P. Sloan Foundation Grant (G-2021-16758) to N.F. and J.D., and a National Science Foundation CAREER Award (PHY-1848247) to N.F.. H.L. and S.G. acknowledge the Gordon and Betty Moore Foundation for support as Physics of Living Systems Fellows through Grant No. GBMF4513. E.K. was supported by the National Science Foundation for a Graduate Research Fellowship under Grant No. DGE 2140743. L.L. was supported by the National Science Foundation for a Graduate Research Fellowship under Grant No. 2141064. J.L. acknowledges the support of the Center for the Physics of Biological Function (PHY-1734030). This research received support through Schmidt Sciences, LLC (to J.D.), the MathWorks Professorship Fund (to J.D.), and National Science Foundation Award DMR-2214021 (to J.D.). N.F. and J.D. thank the WPI-SKCM² Hiroshima University for hospitality and support. The authors acknowledge the MIT SuperCloud and Lincoln Laboratory Supercomputing Center for providing HPC resources that have contributed to the research results reported within this paper.

SUPPLEMENTARY MATERIAL

Materials and methods are provided in the Supplementary Information.

[1] D. Needleman and Z. Dogic, Active matter at the interface between materials science and cell biology, *Nature Reviews Materials* **2**, 1 (2017).

[2] M. C. Marchetti, J.-F. Joanny, S. Ramaswamy, T. B. Liverpool, J. Prost, M. Rao, and R. A. Simha, Hydrodynamics of soft active matter, *Reviews of Modern Physics* **85**, 1143 (2013).

[3] T. Vicsek, A. Czirók, E. Ben-Jacob, I. Cohen, and O. Shochet, Novel type of phase transition in a system of self-driven particles, *Physical Review Letters* **75**, 1226 (1995).

[4] M. Ballerini, N. Cabibbo, R. Candelier, A. Cavagna, E. Cisbani, I. Giardina, V. Lecomte, A. Orlandi, G. Parisi, A. Procaccini, *et al.*, Interaction ruling animal collective behavior depends on topological rather than metric distance: Evidence from a field study, *Proceedings of the National Academy of Sciences* **105**, 1232 (2008).

[5] K. Drescher, K. C. Leptos, I. Tuval, T. Ishikawa, T. J. Pedley, and R. E. Goldstein, Dancing volvox: hydrodynamic bound states of swimming algae, *Physical review letters* **102**, 168101 (2009).

[6] R. Hartmann, P. K. Singh, P. Pearce, R. Mok, B. Song, F. Díaz-Pascual, J. Dunkel, and K. Drescher, Emergence of three-dimensional order and structure in growing biofilms, *Nature Physics* **15**, 251 (2019).

[7] T. Ishikawa, T. Pedley, K. Drescher, and R. E. Goldstein, Stability of dancing volvox, *Journal of Fluid Mechanics* **903**, A11 (2020).

[8] S. Liu, Y. Li, Y. Wang, and Y. Wu, Emergence of large-scale mechanical spiral waves in bacterial living matter, *Nature Physics* **20**, 1015 (2024).

[9] B. von der Heyde, A. Srinivasan, S. K. Birwa, E. L. von der Heyde, S. S. Höhn, R. E. Goldstein, and A. Hallmann, Spatiotemporal distribution of the glycoprotein pherophorin ii reveals stochastic geometry of the growing ecm of volvox carteri, *Proceedings of the National Academy of Sciences* **122**, e2425759122 (2025).

[10] F. Giavazzi, M. Paoluzzi, M. Macchi, D. Bi, G. Scita, M. L. Manning, R. Cebriño, and M. C. Marchetti, Flocking transitions in confluent tissues, *Soft Matter* **14**, 3471 (2018).

[11] W. Tang, A. Das, A. F. Pegoraro, Y. L. Han, J. Huang, D. A. Roberts, H. Yang, J. J. Fredberg, D. N. Kotton, D. Bi, *et al.*, Collective curvature sensing and fluidity in three-dimensional multicellular systems, *Nature Physics* **18**, 1371 (2022).

[12] A. Bricard, J.-B. Caussin, N. Desreumaux, O. Dauchot, and D. Bartolo, Emergence of macroscopic directed motion in populations of motile colloids, *Nature* **503**, 95 (2013).

[13] J. Veenstra, O. Gamayun, X. Guo, A. Sarvi, C. V. Meinersen, and C. Coulais, Non-reciprocal topological solitons in active metamaterials, *Nature* **627**, 528 (2024).

[14] J. J. Hopfield, Neural networks and physical systems with emergent collective computational abilities., *Proceedings of the National Academy of Sciences* **79**, 2554 (1982).

[15] W. F. Paxton, K. C. Kistler, C. C. Olmeda, A. Sen, S. K. St. Angelo, Y. Cao, T. E. Mallouk, P. E. Lammert, and V. H. Crespi, Catalytic nanomotors: autonomous movement of striped nanorods, *Journal of the American Chemical Society* **126**, 13424 (2004).

[16] J. Yan, M. Han, J. Zhang, C. Xu, E. Luijten, and S. Granick, Reconfiguring active particles by electrostatic imbalance, *Nature Materials* **15**, 1095 (2016).

[17] S. A. Mallory, C. Valeriani, and A. Cacciuto, An active approach to colloidal self-assembly, *Annual Review of Physical Chemistry* **69**, 59 (2018).

[18] C. Scheibner, A. Souslov, D. Banerjee, P. Surówka, W. T. Irvine, and V. Vitelli, Odd elasticity, *Nature Physics* **16**, 475 (2020).

[19] C. H. Meredith, P. G. Moerman, J. Groenewold, Y.-J. Chiu, W. K. Kegel, A. van Blaaderen, and L. D. Zarzar, Predator-prey interactions between droplets driven by non-reciprocal oil exchange, *Nature Chemistry* **12**, 1136 (2020).

[20] R. Soto and R. Golestanian, Self-assembly of catalytically active colloidal molecules: tailoring activity through surface chemistry, *Physical Review Letters* **112**, 068301 (2014).

[21] S. Saha, J. Agudo-Canalejo, and R. Golestanian, Scalar active mixtures: The nonreciprocal cahn-hilliard model, *Physical Review X* **10**, 041009 (2020).

[22] Z. You, A. Baskaran, and M. C. Marchetti, Nonreciprocity as a generic route to traveling states, *Proceedings of the National Academy of Sciences* **117**, 19767 (2020).

[23] M. Fruchart, R. Hanai, P. B. Littlewood, and V. Vitelli, Non-reciprocal phase transitions, *Nature* **592**, 363 (2021).

[24] G. Pisegna, S. Saha, and R. Golestanian, Emergent polar order in nonpolar mixtures with nonreciprocal interactions, *Proceedings of the National Academy of Sciences* **121**, e2407705121 (2024).

[25] R. Mandal, S. S. Jaramillo, and P. Sollich, Robustness of traveling states in generic nonreciprocal mixtures, *Physical Review E* **109**, L062602 (2024).

[26] J. Chen, X. Lei, Y. Xiang, M. Duan, X. Peng, and H. Zhang, Emergent chirality and hyperuniformity in an active mixture with nonreciprocal interactions, *Physical Review Letters* **132**, 118301 (2024).

[27] L. Parkavousi, N. Rana, R. Golestanian, and S. Saha, Enhanced stability and chaotic condensates in multispecies nonreciprocal mixtures, *Physical Review Letters* **134**, 148301 (2025).

[28] T. Markovich and T. C. Lubensky, Nonreciprocity and odd viscosity in chiral active fluids, *Proceedings of the National Academy of Sciences* **121**, e2219385121 (2024).

[29] A. Dinelli, J. O’Byrne, A. Curatolo, Y. Zhao, P. Sollich, and J. Tailleur, Non-reciprocity across scales in active mixtures, *Nature Communications* **14**, 7035 (2023).

[30] S. Osat and R. Golestanian, Non-reciprocal multifarious self-organization, *Nature Nanotechnology* **18**, 79 (2023).

[31] F. Brauns and M. C. Marchetti, Nonreciprocal pattern formation of conserved fields, *Physical Review X* **14**, 021014 (2024).

[32] K. L. Kreienkamp and S. H. Klapp, Nonreciprocal alignment induces asymmetric clustering in active mixtures, *Physical Review Letters* **133**, 258303 (2024).

[33] S. Guillet, A. Poncet, M. Le Blay, W. T. Irvine, V. Vitelli, and D. Bartolo, Melting of nonreciprocal solids: How dislocations propel and fission in flowing crystals, *Proceedings of the National Academy of Sciences* **122**, e2412993122 (2025).

[34] S. Kole, X. Chao, A. Mauleon-Amieva, R. Hanai, C. P. Royall, and T. B. Liverpool, Non-reciprocal interactions drive emergent chiral crystallites, *arXiv preprint arXiv:2501.15996* (2025).

[35] S. A. Loos and S. H. Klapp, Irreversibility, heat and information flows induced by non-reciprocal interactions, *New Journal of Physics* **22**, 123051 (2020).

[36] M. J. Bowick, N. Fakhri, M. C. Marchetti, and S. Ramaswamy, Symmetry, thermodynamics, and topology in active matter, *Physical Review X* **12**, 010501 (2022).

[37] T. H. Tan, A. Mietke, J. Li, Y. Chen, H. Higinbotham, P. J. Foster, S. Gokhale, J. Dunkel, and N. Fakhri, Odd dynamics of living chiral crystals, *Nature* **607**, 287 (2022).

[38] Y.-C. Chao, S. Gokhale, L. Lin, A. Hastewell, A. Bacanu, Y. Chen, J. Li, J. Liu, H. Lee, J. Dunkel, *et al.*, Selective excitation of work-generating cycles in nonreciprocal living solids, *arXiv preprint arXiv:2410.18017* (2024).

[39] S. Zhang, C. Fei, and J. Dunkel, Nonlinear memory in cell division dynamics across species, *arXiv preprint arXiv:2408.14564* (2024).

[40] C. Zuo, C. Fei, A. E. Cohen, S. Kim, R. T. Carde, J. Dunkel, and D. L. Hu, Predicting mosquito flight be-

havior using bayesian dynamical systems learning, arXiv preprint arXiv:2505.13615 (2025).

[41] D. J. Skinner, H. Jeckel, A. C. Martin, K. Drescher, and J. Dunkel, Topological packing statistics of living and nonliving matter, *Science Advances* **9**, eadg1261 (2023).

[42] D. J. Skinner, B. Song, H. Jeckel, E. Jelli, K. Drescher, and J. Dunkel, Topological metric detects hidden order in disordered media, *Physical Review Letters* **126**, 048101 (2021).

Supplementary Information:
Topological flowscape reveals state transitions in nonreciprocal living matter

Hyunseok Lee^{1,6}, EliseAnne Koskelo^{1,2,6}, Shreyas Gokhale^{1,6}, Junang Li^{3,6}, Chenyi Fei⁴,
 Chih-Wei Joshua Liu¹, Lisa Lin¹, Jörn Dunkel⁴, Dominic J Skinner⁵, and Nikta Fakhri^{1*}

¹ Department of Physics, Massachusetts Institute of Technology, Cambridge, MA, USA

² Department of Physics, Harvard University, Cambridge, MA, USA

³ Center for the Physics of Biological Function, Princeton University, Princeton, NJ, USA

⁴ Department of Mathematics, Massachusetts Institute of Technology, Cambridge, MA, USA

⁵ Center for Computational Biology, Flatiron Institute, New York, NY, USA

⁶ These authors contributed equally and are joint first authors.

CONTENTS

I. Experimental methods and image analysis	3
A. Preparation of starfish embryos	3
B. Binary pair experiment	3
1. Top-view experiment, image segmentation and tracking	3
2. Side-view experiment, image segmentation and tilt quantification	4
3. Asymmetric precession underlies nonreciprocity between E1 and E2	4
C. Binary mixture experiment	5
1. Mixture experiment, image segmentation and tracking	5
2. Machine learning classification of E1 and E2 embryos	5
3. Velocity polarization rotates clockwise during the traveling state	6
4. E2 embryos lead E1 embryos in collective translation during the traveling state	6
5. Many-body behaviors beyond velocity polarization	6
D. Emergent collective states from additional experiments	8
Demixed LCC	9
Orbiting mixture	9
II. Interaction inference	11
A. All inferred interactions beyond inter-type, longitudinal interactions	12
B. Inferred nonreciprocity between E1-E2 pairs decreases over time	12
III. Model analysis	14
A. Inference-based model of pairwise interactions with tunable nonreciprocity \mathcal{N}	14
B. Implementation of numerical simulations	14
C. Neighbor exchanges become frequent at $\mathcal{N} = 1$	15
IV. Topological metric and structural order parameter	16
A. What is a motif?	16
B. Identification of topological motifs from data	16
C. Calculation of structural order parameter	18
D. Nonreciprocal self-healing	19
V. Topological landscape	21
A. Defining a low-dimensional manifold from topological flipgraph via multidimensional scaling	21
B. Mapping frequency of motifs to probabilities on the manifold via kernel density estimation	21
C. Atlas of topological motifs in simulation and experiment	22

* Corresponding author: fakhri@mit.edu

D. Spatiotemporal distributions of topological motifs M_1 and M_2	23
E. Transition between M_1 and M_2 in experiment is indirect	23
VI. Topological flowscape	
A. Conceptual basis of the flowscape	25
B. Details of topological flowscape introduced in the main text	26
C. Flowscape of inference-based model over the change in nonreciprocity	26
D. Characterization of the transition state	27
E. Motif cycles in cluster merging and fragmentations	27
F. Topological flowscape of additional experiments	27
1. Demixed LCC	27
2. Orbiting mixture	28
VII. Additional analysis	
A. Estimation of entropy production rate	31
B. Information rate over time exhibits a rate transition	32
C. Topological earth mover distance in the main experiment	32
References	34

I. EXPERIMENTAL METHODS AND IMAGE ANALYSIS

A. Preparation of starfish embryos

Starfish (*Patiria miniata*) were obtained from Marinus Scientific and maintained in a saltwater aquarium at 15°C. They were fed shrimp biweekly. Prior to fertilization, we extracted gonads (oocytes and sperm for female and male starfish, respectively) via small incisions on the underside of the adult starfish near the stomach. Spermatophores were stored in Eppendorf tubes at 4°C before use. Ovaries were dissected with scissors to release oocytes, which were then washed once in calcium-free seawater to prevent premature maturation, followed by two rinses in filtered seawater (FSW). The cleaned oocytes were plated as monolayers into multiple sterilized 6-well culture plates (VWR, Catalog Number 10861-554) filled with FSW.

For fertilization, 10mM 1-methyladenine (1-MA) was added to the oocyte cultures at a 1:1000 ratio with FSW. Most oocytes exhibited nuclear envelope breakdown within one hour, which was verified using a dissection microscope (Nikon SMZ745T). Within 2 hours of 1-MA addition, we introduced sperm to the oocyte cultures at an approximate ratio of 10 sperm per oocyte. Fertilized embryos were incubated at 15°C for 24 hours before being transferred to room temperature (approx. 20°C) for subsequent experiments.

After 24 hours, successfully developed embryos began to swim and accumulated at the air-water interface. Only these embryos were collected and transferred into individual wells of a sterilized 24-well tissue culture plate (VWR, Catalog Number 10861-558; single well diameter: 15.7 mm). Each well contained about 2,000–3,000 embryos in 2 mL of FSW.

E1 and E2 embryos were both derived from the same starfish. However, E2 embryos were fertilized 24 hours before the E1 embryos and were kept at 15°C in the interim.

B. Binary pair experiment

To identify pairwise nonreciprocity and the underlying connections to tilt precession dynamics, we performed image analysis of isolated E1-E2 pairs.

1. Top-view experiment, image segmentation and tracking

After the preparation of embryos, 30–50 embryos were transferred into each well of the 24-well plate. Once the microscope was focused on a field of view containing a pair of E1 and E2 embryos, time-lapse videos were captured at a frame rate of 10 frames per second and 1.25X magnification using the dissection scope (Nikon SMZ745T).

We used **Cellpose** [1, 2], a deep learning-based segmentation tool, to identify and segment the pair of starfish embryos (E1 and E2) in each top-view image, applying the “cyto3” pre-trained model. To track the embryos over time, we utilized **Trackpy** [3, 4], adjusting the parameters to reconstruct embryo trajectories from many-embryo snapshots. Key parameters included the search range (maximum distance an object could move between frames) and the memory parameter (maximum number of consecutive missing frames allowed for linking trajectories).

Gaps in the tracked embryo trajectories were filled using trajectory interpolation with the MATLAB function **interp1** and the **pchip** option, which applies shape-preserving cubic spline interpolation. If the number of missing frames at the endpoints was less than the memory parameter, extrapolation was performed to extend the trajectories.

To estimate the tilt direction of embryos from top-view images, we identified the location of blastopores with the MATLAB function **circlefind**. When the AP axis is tilted, the top-view centroid position of the embryo deviates from the position of blastopore, and we use the direction from the blastopore to the centroid as a proxy for direction of the AP axis (Fig. S1a).

2. Side-view experiment, image segmentation and tilt quantification

To capture side-view images of starfish embryos, we pipetted the swimming embryos into a 25 mL tissue culture flask. The flask was positioned between the objective and the light source of a dissection microscope placed on its side. The images were taken at 10 frames per second and at 4X magnification.

As in the top-view experiments, we used **Cellpose** with the “cyto3” pre-trained model. Segmentation fitted each embryo’s side-view snapshot to an ellipsoid, and we used the direction of the major axis to estimate the tilt of the AP axis from an upright position.

3. Asymmetric precession underlies nonreciprocity between E1 and E2

We find that starfish embryos at different developmental stages, E1 and E2, exhibit nonreciprocal interactions through a run-and-chase dynamic, where E1-E2 pairs drift toward the E2 embryo. This is perhaps expected, as inter-embryo interactions are mediated by self-generated hydrodynamic flows that evolve with developmental stage [5]. Nonetheless, identifying a clear mechanistic basis for E1-E2 nonreciprocity can provide insight into the underlying physics and inform the design of synthetic nonreciprocal systems. To this end, we propose a mechanism for nonreciprocity that emphasizes the inherently three-dimensional nature of the embryo system.

In water, starfish embryos self-propel along their anterior-posterior (AP) axis due to their ciliary beating, while simultaneously rotating clockwise around this axis. At the air-water interface, their upward self-propelling force counteracts gravity, allowing the embryos to remain bounded at the surface. In a symmetric setup, the AP axis would be oriented upright, perpendicular to the interface. However, in E1-E2 pairs, this symmetry can be broken, leading to a biased tilt of the AP axis.

Our experiments show that the observed nonreciprocity between E1 and E2 is consistent with this biased tilt. Specifically, we find that the pairwise nonreciprocity oscillates over time, as indicated by a run-and-chase dynamic, and reaches a maximum when E2 is tilted away from E1 (Fig. S1a), suggesting that E2’s self-propulsion along its tilted AP axis influences the pair dynamics. If E2’s tilt were symmetric over time, its net contribution to the dynamics would average to zero. However, side-view imaging reveals an asymmetric tilt: E2 tilts more strongly when directed away from E1 (Fig. S1b). Taken together, these results indicate that the asymmetric tilt of E2’s AP axis plays a key role in driving the observed nonreciprocal interaction between E1 and E2.

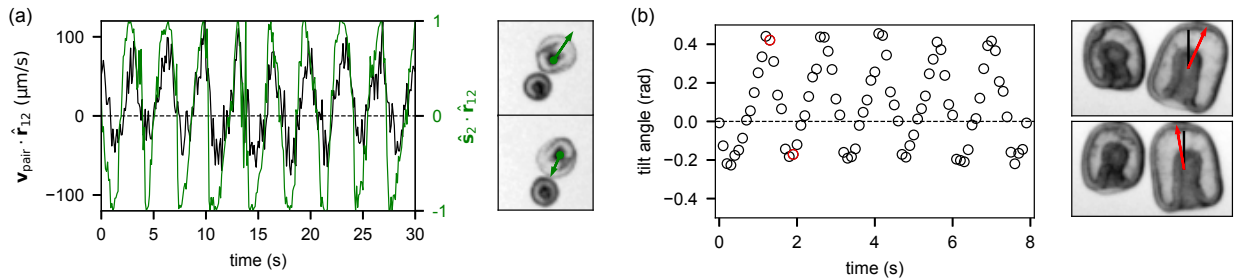


FIG. S1. Asymmetric tilt of E2’s AP axis contributes to nonreciprocity between E1 and E2. (a) Left: Time series of the drift speed toward E2 (black) and E2’s morphology polarization $\hat{\mathbf{s}}$ ’s alignment with $\hat{\mathbf{r}}_{12} \equiv \frac{\mathbf{r}_2 - \mathbf{r}_1}{|\mathbf{r}_2 - \mathbf{r}_1|}$ (green). Right: Estimation of $\hat{\mathbf{s}}$ (green arrow) from a displacement from blastopore (black dot) to centroid of E2 embryo images. The drift speed increases when E2 is tilted away from E1, indicating that E2’s self-propulsion along its tilted AP axis significantly contributes to the nonreciprocal interaction. (b) E2’s tilt is asymmetric; it tilts more strongly when oriented away from E1 than toward it. Note: the embryo pair shown in **B** is different from that in **A**, and the oscillation period differs accordingly [5].

C. Binary mixture experiment

1. Mixture experiment, image segmentation and tracking

After the preparation of embryos, 2000–3000 embryos were transferred to a single well of the 24-well plate. The ratio of E1 to E2 embryos was kept approximately equal, with 1,000–1,500 E1 embryos and 1,000–1,500 E2 embryos. The total volume was maintained at 2 mL.

Time-lapse videos were captured at a frame rate of one frame every 5 seconds. Imaging was performed using a dissection microscope (Nikon SMZ745) equipped with a high-speed CMOS digital camera (Amscope MU500) mounted at the eyepiece.

We used **Cellpose** [1, 2], a deep learning-based segmentation tool, to identify and segment individual starfish embryos in each top-view image. The “cyto2” pre-trained model was applied, with the embryo diameter set as $23\ \mu\text{m}$ to guide the model.

Unlike the pair experiments where we could easily identify the tracks of E1 and tracks of E2, we needed a new way to classify the embryos based on their development stages. We describe the method in the next section.

2. Machine learning classification of E1 and E2 embryos

As the mixed experiment contains a large number of embryos, we trained a machine learning model to classify embryos as either E1 (24 hours post fertilization) or E2 (48 hours post fertilization). The model training set initially comprised crops around all embryo positions found by **Trackpy** [3, 4] in snapshots of a living chiral crystal (LCC) [5]. This experiment (LCC) consists of embryos from a single developmental stage that remained in the field of view for a long enough time span including both 24 hours post fertilization and 48 hours post fertilization, which allowed us to label crops of the 24 hours post fertilization snapshot as class E1 and crops of the 48 hours post fertilization snapshot as class E2. Model test sets initially comprised the sequences of crops around all embryo positions found by **Cellpose** [1, 2] from the mixed experiment. Each crop sequence contained all observations of a single embryo. Crops were preprocessed in **scikit-image** [6] by rolling-ball background subtraction [7] using a ball radius of 8 pixels followed by CLAHE (contrast limited adaptive histogram equalization) [8]. All crops were 32×32 pixels. Crops around embryo positions not fully in the field of view (within 16 pixels of the boundary of LCC-snapshot or mixture experiment snapshot) were excluded from classification analyses. Training datasets were balanced by randomly dropping crops of the majority class. The final training dataset contained $N = 2792$ observations with 1396 of each class.

A random forest [9] of 100 decision trees was then trained using the **RandomForestClassifier** class from the **scikit-learn** [10] Python package. All hyperparameters were set to defaults except the random state, which was set to 1234. Each decision tree was trained on a bootstrap sample of size N from the training dataset. Splits were chosen using the CART (classification and regression tree) algorithm [11] by greedily decreasing the Gini impurity [12]. During a growth step, 32 randomly chosen features (pixels) were considered at each leaf: the pixel threshold that most decreased the Gini impurity was used to split observations at the leaf into two new leaves. Trees were grown until all leaves were pure (contained observations of only one class). Pure leaves were assigned to the class of their observations. During prediction, individual decision trees assigned each test-set crop to a leaf (hard class label) using the splits learned during training. The proportions of the 100 trees assigning a crop to an E1 or E2 leaf were then assigned as the E1 or E2 class probabilities (soft labels) of the crop. Class probabilities were averaged over all crops in a sequence, and the embryo imaged in the sequence was finally classified as belonging to the class (E1 or E2) with the highest average probability.

Evaluation using 970 manually labeled binary-mixture embryos with correct tracks of at least 30 observations revealed an accuracy of 0.959 (Clopper-Pearson 0.95 CI [13]: [0.944, 0.970]).

3. Velocity polarization rotates clockwise during the traveling state

In the main text Fig. 1d, we show velocity polarization components \mathbf{P}_x and \mathbf{P}_y . During the traveling state, the two components show oscillatory behavior with a time lag. Here, we show the direction of velocity polarization $\phi_{\mathbf{P}} \equiv \arctan(\mathbf{P}_y/\mathbf{P}_x)$. The time series of $\phi_{\mathbf{P}}$ shows a constant decline, indicating a clockwise rotation of the direction that embryos collectively flock toward (Fig. S2).

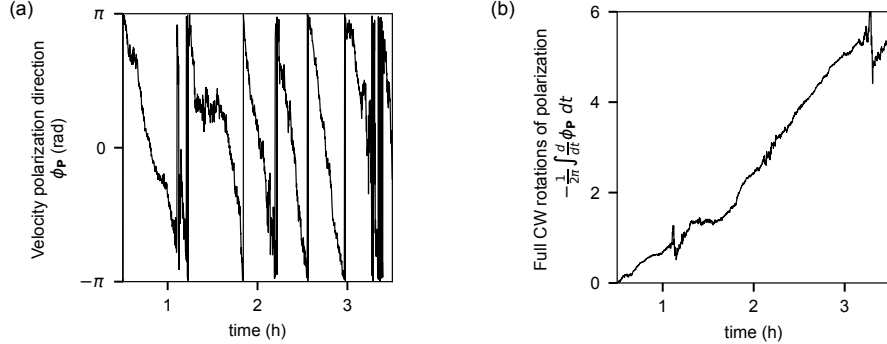


FIG. S2. **Velocity polarization rotates clockwise during the traveling state.** (a) Time series of $\phi_{\mathbf{P}} \equiv \arctan(\mathbf{P}_y/\mathbf{P}_x)$, the direction of velocity polarization \mathbf{P} . (b) Cumulative number of full clockwise rotations of \mathbf{P} , starting from 0.5h in the experiment.

4. E2 embryos lead E1 embryos in collective translation during the traveling state

In theory, the nonreciprocity-driven emergent polar order, such as traveling wave in mixed populations, should exhibit spatial asymmetry that reflects underlying run-and-chase dynamics. In our system, where E2 embryos “run” from E1, we expect E2 to consistently lead the traveling wave, with E1 following behind.

Although the direction of velocity polarization \mathbf{P} changes over time, it does so in a predictable manner: the direction rotates clockwise. This allows us to identify the leading population at any moment by examining which embryo types are ahead in this rotation. Specifically, embryos with $\phi_{\mathbf{v}} - \phi_{\mathbf{P}} < 0$ (i.e., those rotated clockwise from \mathbf{P}) are leading in the direction of collective motion.

To further quantify which population leads, we define a global order parameter, the type-weighted position vector:

$$\psi_q \equiv \sum_i q_i (\mathbf{r}_i - \frac{1}{N} \sum_j \mathbf{r}_j), \quad (1)$$

where $q_i = 1$ for E2 and $q_i = -1$ for E1. For a single E1-E2 pair, this reduces to $\mathbf{r}_{12} \equiv \mathbf{r}_2 - \mathbf{r}_1$. For greater than two embryos, ψ_q points toward regions enriched in E2 and depleted of E1. We compare the alignment between ψ_q and the average velocity $\langle \mathbf{v}_i \rangle_i$ to evaluate whether collective motion is biased toward E2.

Together, these two independent analyses confirm that E2 embryos consistently lead E1 in the collective flocking during the traveling state (Fig. S3).

5. Many-body behaviors beyond velocity polarization

In the main text, we focus on the velocity polarization $\mathbf{P} \equiv \langle \hat{\mathbf{v}} \rangle$, as a key signature of collective behavior in the embryo system. However, this is not the only emergent feature observed. In this section, we describe additional aspects of the many-body dynamics seen in the experiment.

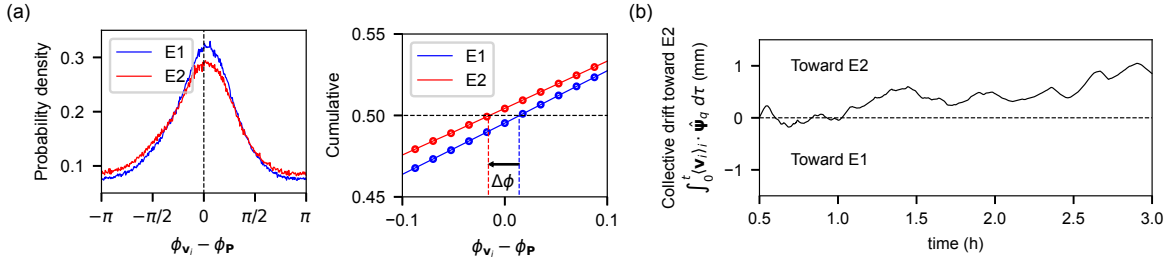


FIG. S3. **E2 embryos lead E1 embryos in collective translation during the traveling state.** (a) Probability and cumulative distributions of $\phi_{v_i} - \phi_{\mathbf{P}}$, the angular deviation of each embryo's velocity direction from the global velocity polarization \mathbf{P} . E2 embryos are, on average, rotated slightly clockwise relative to E1s, with a median angular lead of $\Delta\phi = 0.03$ rad. Given that $\phi_{\mathbf{P}}$ rotates approximately 2.5 times per hour, this corresponds to a temporal lead of about 7 seconds for E2s in the flocking dynamics. (b) Collective biased drift analogous to the pairwise biased drift shown in Fig. 1b. We define a type-weighted position vector $\psi_q \equiv \sum_i q_i (\mathbf{r}_i - \frac{1}{N} \sum_j \mathbf{r}_j)$, with $q_i = \pm 1$ for E2 and E1, respectively. Integrating the projection of average system velocity $\langle \mathbf{v}_i \rangle_i$ onto ψ_q over time confirms that the velocity polarization \mathbf{P} is biased toward the E2-rich direction.

At the start of the experiment (time 0), we mix thousands of E1 and E2 embryos. Some embryos quickly rise to the air-water interface, while others remain submerged. Over the first 30 minutes, the number of embryos visible at the interface increases rapidly, then plateaus around 1 hour (Fig. S4). For consistency across measurements, we set the start time for analysis in the main text as 30 minutes after mixing (i.e., 0.5 h).

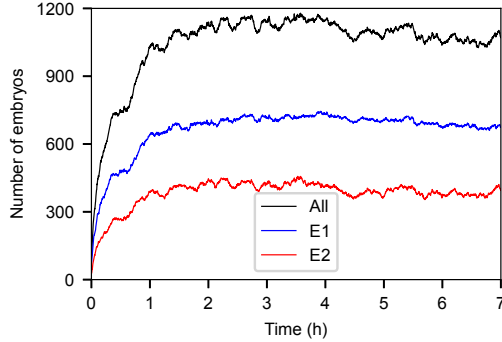


FIG. S4. **Time series of the number of embryos at the air-water interface**

For the first three hours of the experiment (the traveling state), the embryos exhibit persistent collective translation (Fig. 1d). During this phase, they also form transient clusters that continuously break and merge. This dynamic structural organization is quantified using the hexatic order parameter, $\psi_6 = \frac{1}{n} \sum_{i=1}^n e^{6i\theta_i}$, where θ_i is the angle to the i th nearest neighbor. A value of $|\psi_6| = 1$ corresponds to perfect hexagonal packing, i.e., six neighbors separated by $\pi/3$. Interestingly, E1 embryos tend to have higher $|\psi_6|$ values than E2 (Fig. S5a), and are also more likely to have exactly six neighbors (Fig. S5b). In addition, E1 embryos generally move more slowly than E2 embryos (Fig. S5c). Together, these findings suggest that E1s are more structurally ordered and less dynamic than E2s during the traveling state.

Despite these differences, both E1 and E2 embryos exhibit similar velocity autocorrelation functions in the traveling state (Fig. S5d), including a shared negative peak in the cross-correlation $\langle \hat{\mathbf{v}}(t) \times \hat{\mathbf{v}}(t + \tau) \rangle_z = \langle v_x(t)v_y(t + \tau) - v_y(t)v_x(t + \tau) \rangle$, which reflects the clockwise chirality of their trajectories. This indicates that, at long timescales, both types of embryos' long-time dynamics are governed by the same collective translation of the system.

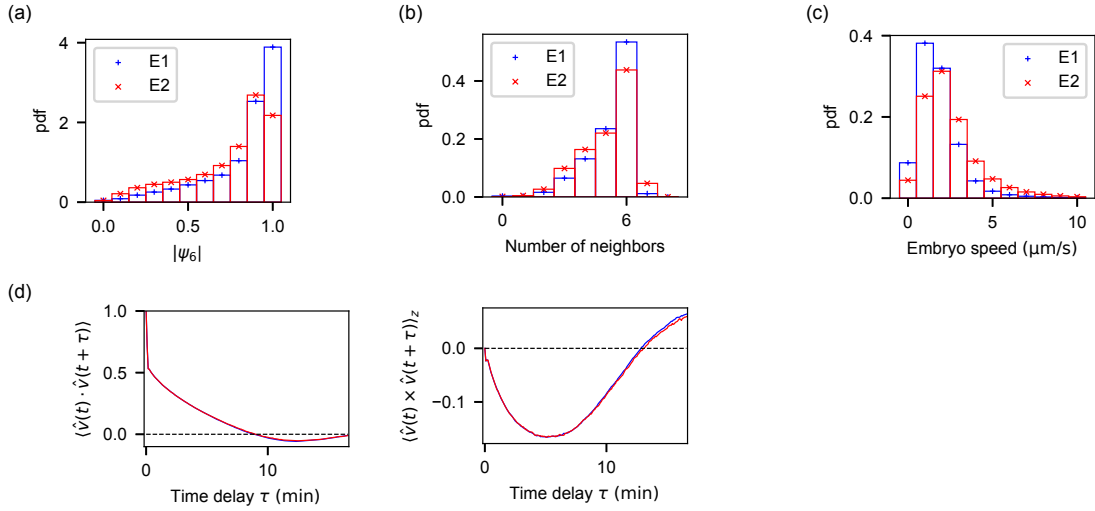


FIG. S5. Statistical differences between E1 and E2 embryos during the traveling state. (a) Distribution of the magnitude of the hexatic order parameter $|\psi_6|$. E1 embryos tend to exhibit higher structural order than E2. (b) Distribution of the number of neighbors. E1 embryos are more likely to have exactly six neighbors. (c) Distribution of embryo speeds. E1 embryos move more slowly on average than E2. (d) Velocity autocorrelation functions for E1 (blue) and E2 (red). Both types show similar temporal correlations in both longitudinal and transverse directions, persisting over several minutes.

In the later hours of the experiment (the fluctuating state), the embryos cease their collective translation and instead self-organize into a more stable, ordered lattice. This transition is captured by the increasing hexatic order parameter $\langle |\psi_6| \rangle$, which quantifies local sixfold symmetry (Fig. S6). Over time, $\langle |\psi_6| \rangle$ rises steadily, indicating the progressive development of structural order in the system (Fig. S6).

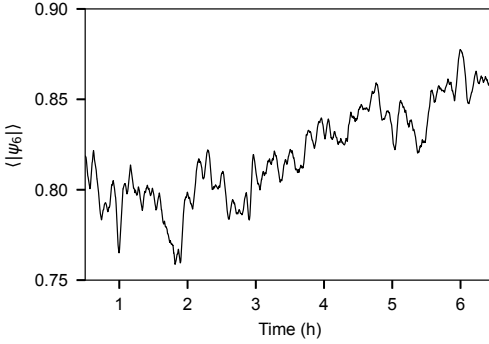


FIG. S6. Emergence of hexatic order in the fluctuating state. Time series of the system-averaged hexatic order parameter $\langle |\psi_6| \rangle$. As the system transitions from the traveling to the fluctuating state, local structural order increases, reflecting the formation of an ordered lattice.

D. Emergent collective states from additional experiments

Compared to a homogeneous embryo system—which typically forms a living chiral crystal (LCC)—the biologically tuned nonreciprocity between E1 and E2 embryos enables access to a much richer set of nonequilibrium behaviors, such as the traveling state discussed in the main text.

Here, we highlight two additional emergent collective states that further demonstrate the versatility of our experimental platform. In both of the additional experiments, unless otherwise noted, we followed the same embryo preparation and data analysis pipeline as described in SI Sec. IC 1.

Demixed LCC

In the main experiment, E1 and E2 embryos are mixed by stirring the well during their addition. However, if we skip this mixing step, the embryos remain initially demixed. Because E2 embryos are developmentally more advanced, they tend to reach the air-water interface earlier than E1 embryos. This results in the early formation of a nearly homogeneous LCC composed mostly of E2 embryos. As time progresses, E1 embryos rise to the interface and attach to the periphery of the existing LCC, driving crystal growth. Eventually, E2 embryos lose stability at the interface and disappear, leading to an E1-dominated LCC. This results in a demixed regime that remains largely crystalline throughout (Fig. S7).

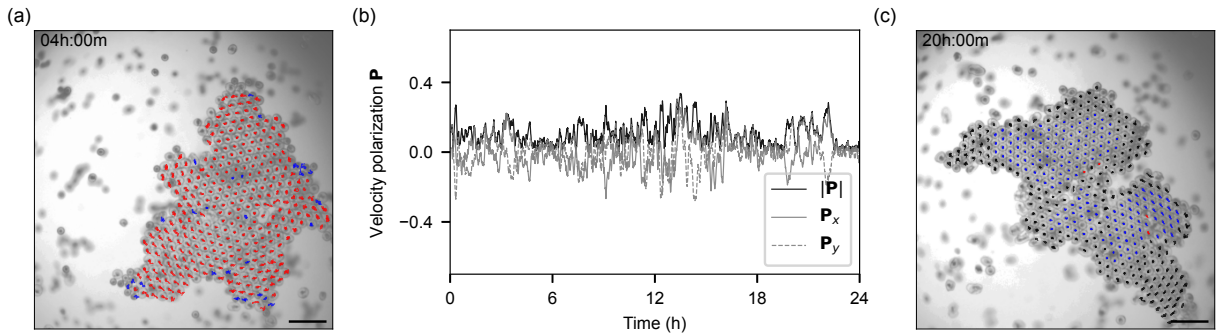


FIG. S7. Snapshots and velocity polarization of demixed LCC. (a) Snapshot of the system shortly after E2 embryos have formed a nearly homogeneous crystal. Snapshot overlaid with 2-minute trajectories (blue: E1, red: E2). (b) Time series of velocity polarization, which remains low and fluctuates over time, indicating a lack of persistent collective motion. (c) Later snapshot showing an E1-dominated LCC after E2 embryos have disappeared. Embryos that appear after the first 12 hours of the experiment are labelled as black; for these embryos with age of 36h or beyond, our classifier based on 24h and 48h embryos may not be applicable. Given that most E2 embryos become unstable at the air-water interface at this point, these embryos that appear later are likely to be E1 embryos.

Orbiting mixture

In the main experiment, the embryos primarily occupy the interior of the well and stay away from the circular boundary. However, if we introduce a significantly larger number of embryos, the system becomes densely packed, extending to the edge of the well. In this boundary-filled configuration, the embryos have little space to separate or break into distinct clusters, unlike in the traveling state. Instead, the entire system undergoes a persistent orbiting motion along the circular boundary, accompanied by continuous internal rearrangements. This high-density configuration gives rise to a distinct collective state: an orbiting mixture (Fig. S8).

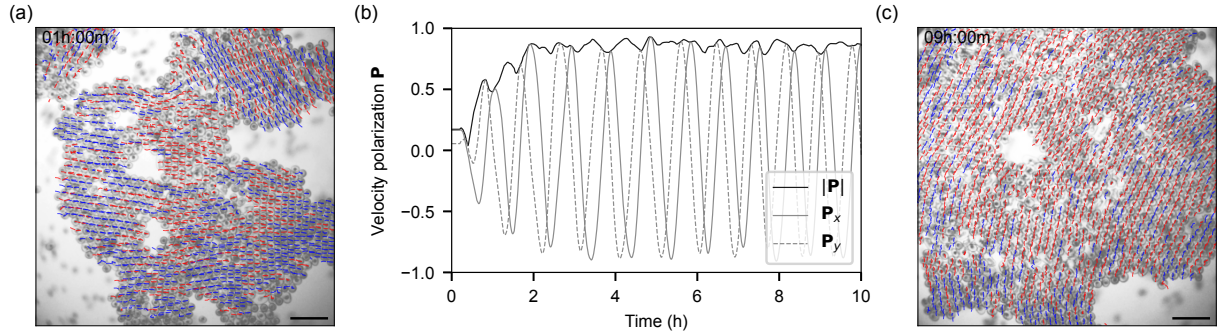


FIG. S8. Snapshots and velocity polarization of orbiting mixture. (a) Initial snapshot of a densely packed embryo system filling the well. Snapshot overlaid with 2-minute trajectories (blue: E1, red: E2). (b) Time series of velocity polarization, which remains close to 1, indicating persistent, coherent translation along the boundary. (c) Later snapshot showing continued orbiting motion with internal rearrangements.

II. INTERACTION INFERENCE

To describe the positional dynamics of starfish embryo mixtures, we employ the following equation:

$$\frac{d\mathbf{r}_i}{dt} = \sum_{j \neq i} f_L^{l_i l_j}(r_{ij}) \hat{\mathbf{r}}_{L,ij} + \sum_{j \neq i} f_T^{l_i l_j}(r_{ij}) \hat{\mathbf{r}}_{T,ij} + \boldsymbol{\xi}_i, \quad (2)$$

where \mathbf{r}_i denotes the in-plane coordinates of the i^{th} embryo, l_i denotes the type of the i^{th} embryo ($l_i = 1$ for E1 embryo and $l_i = 2$ for E2 embryo), f_L and f_T denote, respectively, the magnitudes of the longitudinal and transverse interactions, and $\boldsymbol{\xi}_i$ denotes a Gaussian white noise satisfying $\boldsymbol{\xi}_i(t)\boldsymbol{\xi}_j(t') = \Delta\mathbf{I}\delta_{ij}\delta(t-t')$, with Δ a scalar, and \mathbf{I} the identity matrix. Here, the in-plane displacement vector between embryos i and j is given by $\mathbf{r}_{ij} \equiv \mathbf{r}_j - \mathbf{r}_i = r_{ij}\hat{\mathbf{r}}_{ij}$, where r_{ij} is the distance between the embryos and $\hat{\mathbf{r}}_{ij}$ is the unit vector along this direction. Thus, the longitudinal unit vector is given by $\hat{\mathbf{r}}_{L,ij} = \hat{\mathbf{r}}_{ij}$, and the transverse unit vector is given by $\hat{\mathbf{r}}_{T,ij} = \hat{\mathbf{r}}_{ij} \times \hat{\mathbf{z}}$ where the unit vector $\hat{\mathbf{z}}$ is perpendicular to the plane in which the embryos reside.

To infer the force magnitudes f_L and f_T from time series of embryo positions, we parameterize f using basis function expansions:

$$f(r_{ij}) = \sum_n w_n \theta_n(r_{ij}; R_0), \quad (3)$$

where we choose $\theta_n(r_{ij}; R_0) = L_n(r_{ij}/R_0) \exp(-\frac{r_{ij}}{2R_0})$ indicating Laguerre polynomials L_n with an exponential weighting factor, and we aim to learn the coefficients w_n from data. The choice of the scale parameter R_0 will be discussed later. Introducing Eq. (3) into Eq. (2), we obtain:

$$\begin{aligned} \frac{d\mathbf{r}_i}{dt} &= \sum_{j \neq i} \sum_n (w_n)_L^{l_i l_j} \theta_n(r_{ij}) \hat{\mathbf{r}}_{L,ij} + \sum_{j \neq i} \sum_n (w_n)_T^{l_i l_j} \theta_n(r_{ij}) \hat{\mathbf{r}}_{T,ij} + \boldsymbol{\xi}_i \\ &= \sum_{\substack{O=L,T \\ l=E1,E2 \\ l'=E1,E2}} \sum_n (w_n)_O^{ll'} \left[\sum_{j \neq i} \delta_{l_i l} \delta_{l_j l'} \theta_n(r_{ij}) \hat{\mathbf{r}}_{O,ij} \right] + \boldsymbol{\xi}_i \end{aligned} \quad (4)$$

This essentially reduces the inference task to a linear regression problem. We stack the eight sets of $(w_n)_O^{ll'} (O = L, T; l = E1, E2; l' = E1, E2)$ into a coefficient vector \mathbf{w} . Similarly, Eqs. (4) for all embryos at different time points can be stacked together into a matrix form:

$$\mathbf{v} = \boldsymbol{\Theta} \mathbf{w} + \boldsymbol{\xi}, \quad (5)$$

where \mathbf{v} and $\boldsymbol{\xi}$ are velocity and noise vectors in \mathbb{R}^N , $\boldsymbol{\Theta}$ is the library matrix in $\mathbb{R}^{N \times M}$, and \mathbf{w} is the coefficient vector in \mathbb{R}^M . Here, each row corresponds to a spatial dimension of an embryo at a time point, and each column of $\boldsymbol{\Theta}$ corresponds to an interaction mode (O, l, l') and computes the summation in the big square bracket in Eq. (4).

To perform Bayesian inference of \mathbf{w} , we minimize the negative log-posterior:

$$-\ln P(\mathbf{w} | \{\mathbf{r}_i(t)\}) \sim -\ln P(\{\mathbf{r}_i(t)\} | \mathbf{w}) - \ln P(\mathbf{w}) \quad (6)$$

with respect to \mathbf{w} given measurements $\{\mathbf{r}_i(t)\}$. To prevent overfitting, we follow previous work [14, 15] and impose a sparsity-promoting Gaussian prior over the coefficients:

$$P(\mathbf{w}) = \prod_m \mathcal{N}(w_m | 0, \gamma_m) = \prod_m (2\pi\gamma_m)^{-1/2} \exp\left(-\frac{w_m^2}{2\gamma_m}\right), \quad (7)$$

where γ_m are hyperparameters representing the variances of the Gaussian distributions, and we use a single index m to represent the triplets (O, l, l') in Eq. (4). Thus, the negative log-prior reads:

$$-\ln P(\mathbf{w}) = \sum_m \frac{w_m^2}{2\gamma_m} + \sum_m \frac{1}{2} \ln(2\pi\gamma_m), \quad (8)$$

which is similar to an L2 regularization on the weights [16, 17]. The negative log-likelihood function is given by:

$$-\ln P(\{\mathbf{r}_i(t)\}|\mathbf{w}) = \frac{N}{2} \ln(2\pi) + \frac{1}{2} \ln |\boldsymbol{\Psi}| + \frac{1}{2} (\mathbf{v} - \boldsymbol{\Theta}\mathbf{w})^T \boldsymbol{\Psi}^{-1} (\mathbf{v} - \boldsymbol{\Theta}\mathbf{w}), \quad (9)$$

where $\boldsymbol{\Psi} = \Delta \mathbf{I}_N$ assuming Gaussian white noise. Introducing Eqs. (8, 9) into Eq. (6), we obtain the posterior that follows a Gaussian distribution $P(\mathbf{w}|\{\mathbf{r}_i(t)\}) = \mathcal{N}(\mathbf{w}; \boldsymbol{\mu}, \boldsymbol{\Sigma})$, where the covariance matrix $\boldsymbol{\Sigma}$ and the mean $\boldsymbol{\mu}$ are given by:

$$\boldsymbol{\Sigma} = (\boldsymbol{\Theta}^T \boldsymbol{\Psi}^{-1} \boldsymbol{\Theta}^T + \boldsymbol{\Gamma}^{-1})^{-1} \quad (10)$$

$$\boldsymbol{\mu} = \boldsymbol{\Sigma} \boldsymbol{\Theta}^T \boldsymbol{\Psi}^{-1} \mathbf{v}, \quad (11)$$

and $\boldsymbol{\Gamma}$ is a diagonal matrix with $\boldsymbol{\Gamma}_{mm} = \gamma_m$.

To determine the values of hyperparameters in Eqs. (10, 11), we employ a pragmatic procedure based on previous work [18], and choose γ_m and Δ to maximize the marginal likelihood $P(\{\mathbf{r}_i(t)\}|\Delta, \{\gamma_m\}) = \int P(\{\mathbf{r}_i(t)\}|\mathbf{w}; \Delta) P(\mathbf{w}|\{\gamma_m\}) d\mathbf{w}$. We use the Expectation Maximization (EM) method to iteratively update the values of γ_m and Δ . Specifically, given $\gamma_m^{(n)}$ and $\Delta^{(n)}$ from the previous iteration, we compute the current estimate of $\boldsymbol{\mu}^{(n)}$ and $\boldsymbol{\Sigma}^{(n)}$ using Eqs. (10, 11). The EM approach gives the re-estimates:

$$\gamma_m^{(n+1)} = \mathbb{E}_{\mathbf{w} \sim \mathcal{N}(\boldsymbol{\mu}^{(n)}, \boldsymbol{\Sigma}^{(n)})} [\mathbf{w}_m^2] = (\boldsymbol{\mu}_m^{(n)})^2 + \boldsymbol{\Sigma}_{mm}^{(n)}, \text{ and} \quad (12)$$

$$\Delta^{(n+1)} = \mathbb{E}_{\mathbf{w} \sim \mathcal{N}(\boldsymbol{\mu}^{(n)}, \boldsymbol{\Sigma}^{(n)})} \left[\frac{|\mathbf{v} - \boldsymbol{\Theta}\mathbf{w}|^2}{N} \right] = \frac{1}{N} \left[|\mathbf{v} - \boldsymbol{\Theta}\boldsymbol{\mu}^{(n)}|^2 + \Delta^{(n)} \sum_m (1 - \boldsymbol{\Sigma}_{mm}^{(n)} / \gamma_m^{(n)}) \right]. \quad (13)$$

We note that when the degrees of freedom of the data samples N is much larger than the number of modes M , Eq. (13) can be approximated by $\Delta^{(n+1)} \approx |\mathbf{v} - \boldsymbol{\Theta}\boldsymbol{\mu}^{(n)}|^2 / N$. Finally, we note that the scale parameter R_0 is chosen to minimize the residual $|\mathbf{v} - \boldsymbol{\Theta}\boldsymbol{\mu}^{(n)}|^2 / N$ through an additional layer of optimization outside of EM.

A. All inferred interactions beyond inter-type, longitudinal interactions

We infer pairwise interactions between embryos in the binary mixture experiment by applying our inference method to the full trajectory dataset $\{\mathbf{r}_i(t), \dot{\mathbf{r}}_i(t)\}$ over all frames. This procedure yields eight distinct interactions, corresponding to the four embryo-type combinations (E1–E1, E1–E2, E2–E1, E2–E2) and their longitudinal or transverse components, as shown in Fig. S9.

The full set of interactions recapitulates several features of the embryo pairs. First, the longitudinal self-interactions (E1–E1 vs. E2–E2) differ in both magnitude and interaction range, reflecting the larger size of E2 embryos. Second, the transverse interactions are negative at the equilibrium pair distances (195 μm for E1–E1 and 237 μm for E2–E2, based on longitudinal self-interactions), consistent with the observed clockwise rotation of embryo pairs. This transverse component reflects the chiral symmetry breaking arising from the ciliary beating of the embryos.

B. Inferred nonreciprocity between E1–E2 pairs decreases over time

In the main text, we present pairwise interactions inferred from all-time data. Here, we show the nonreciprocity of longitudinal interactions between E1 and E2 embryos in time-segmented inference, where we use data from a segmented time-window (every 500 frames = 2500 seconds) to infer interactions. For each $f_L^{12,21}$ we obtain for a time-segmented data, we identify nonreciprocity $\mathcal{N}(t)$ by fitting $(f_L^{12} - f_L^{21})_t = \mathcal{N}(t) \times (f_L^{12} - f_L^{21})_{\text{all time}}$. Over the course of experiment, inferred nonreciprocity decreases from $\mathcal{N} = 1.2$ to $\mathcal{N} = 0.9$ (Fig. S10).

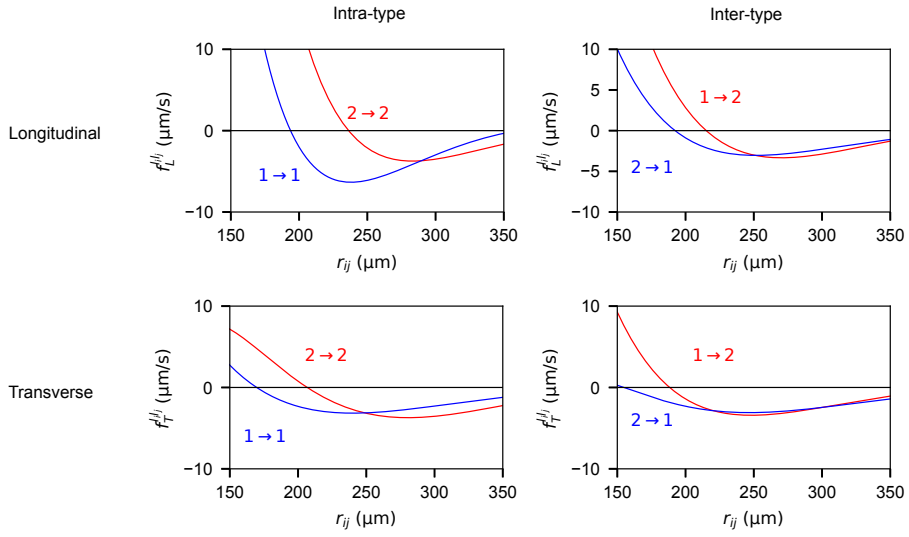


FIG. S9. All inferred interactions beyond inter-type, longitudinal interactions.

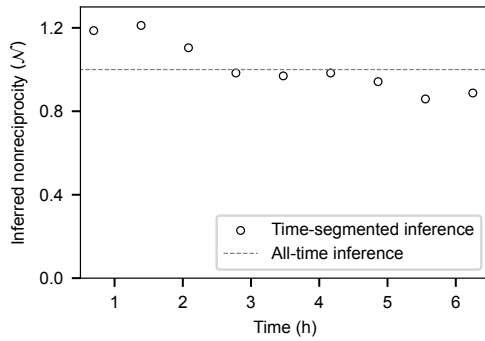


FIG. S10. Inferred nonreciprocity between E1-E2 pairs decreases over time Over the course of experiment, inferred nonreciprocity decreases from $\mathcal{N} = 1.2$ to $\mathcal{N} = 0.9$.

III. MODEL ANALYSIS

A. Inference-based model of pairwise interactions with tunable nonreciprocity \mathcal{N}

We construct a data-driven model based on pairwise interactions inferred from trajectories of starfish embryos. The dynamics of embryo i are modeled as overdamped and governed by effective interactions with all other embryos:

$$\frac{d\mathbf{r}_i}{dt} = \sum_j f_L^{l_i l_j}(r_{ij}) \hat{\mathbf{r}}_{ij} + f_T^{l_i l_j}(r_{ij}) \hat{\mathbf{r}}_{ij} \times \hat{z} - f_r \mathbf{r}_i \quad (14)$$

Here, $\hat{\mathbf{r}}_{ij}$ is the unit vector pointing from embryo i to j , and $l_i \in \{1, 2\}$ denotes the type (E1 or E2) of embryo i . The interaction functions $f_L^{l_i l_j}(r)$ and $f_T^{l_i l_j}(r)$ are the longitudinal and transverse components of the effective force, inferred from the main binary mixture experiment (SI Sec. II). These forces are normalized by embryo drag coefficients, and we assume that inertia is negligible due to strong overdamping. We also neglect noise, based on the assumption that self-generated flows captured by pairwise interactions dominate the embryo dynamics.

To explore how nonreciprocity affects collective behavior, we introduce a one-parameter family of interaction models that systematically vary the degree of asymmetry between E1-E2 interactions. Specifically, we only modify the longitudinal interaction terms $f_L^{12}(r)$ and $f_L^{21}(r)$, while keeping all other interaction functions fixed at their experimentally inferred values.

To enable this, we decompose the inferred E1-E2 longitudinal interactions into symmetric and antisymmetric parts:

$$f_L^S(r) \equiv \frac{f_L^{12}(r) + f_L^{21}(r)}{2}, \quad f_L^A(r) \equiv \frac{f_L^{12}(r) - f_L^{21}(r)}{2} \quad (15)$$

We then construct a tunable model with nonreciprocity parameter \mathcal{N} as:

$$f_L^{12}(r; \mathcal{N}) = f_L^S(r) + \mathcal{N} f_L^A(r), \quad f_L^{21}(r; \mathcal{N}) = f_L^S(r) - \mathcal{N} f_L^A(r) \quad (16)$$

This form ensures that the system is reciprocal when $\mathcal{N} = 0$, and matches the inferred interactions when $\mathcal{N} = 1$. We explore a range of values including weaker ($\mathcal{N} < 1$) and stronger ($\mathcal{N} > 1$) nonreciprocity to isolate its effect on emergent behaviors.

To mimic the curved air-water interface of the experimental system, as reported in [5], we introduce a weak central potential term, modeled by $f_r = 2 \times 10^{-4}$. For embryos within 10 interaction units of the center, the magnitude of this confinement force is approximately three orders of magnitude weaker than a typical pairwise interaction. This central potential prevents embryos from drifting arbitrarily far, capturing the effect of the confining geometry of the experimental well. Additionally, we reduce the strength of transverse interactions f_T to 10% of the inferred values, reflecting the size-dependent slowdown of cluster rotations reported in [5].

B. Implementation of numerical simulations

We implemented the model in Julia and performed simulations using a forward Euler method with a time step of $\Delta t = 0.1$ model time unit. Based on the experimental distribution of embryo displacement per frame (relative to distance between embryos), we record simulation snapshots every 7.5 model time units (75 time steps). Simulations were run in an open domain without periodic or reflective boundaries. Although the domain was unbounded, the weak central potential was sufficient to confine the dynamics within a finite area, as observed experimentally.

We explored nine levels of nonreciprocity, $\mathcal{N} \in \{0, 0.25, 0.5, 0.75, 1, 1.25, 1.5, 1.75, 2\}$, and ran 20 independent simulations for each value. Each simulation was initialized with 200 E1 and 200 E2 embryos placed randomly within a square domain of size $[-20, 20] \times [-20, 20]$, where one unit length corresponds to $267 \mu\text{m}$.

Each simulation was run for 3000 frames. To remove transient effects, we analyzed only the second half of each trajectory (frames 1501-3000). For these data, we computed time-averaged metrics including velocity polarization \mathbf{P} , the structural order parameter $\langle d_{\text{hex}} \rangle$, and the frequency of topological motifs, which together characterize collective motion and spatial organization.

All simulations were performed on the MIT Supercloud cluster using Julia v1.9.1. We verified that results are compatible with Julia v1.11, and that all package dependencies are reproducible and documented.

C. Neighbor exchanges become frequent at $\mathcal{N} = 1$

Our inference-based simulations reveal that sufficiently strong nonreciprocity disrupts crystalline order, producing repeated cycles of cluster merging and breaking. To quantify this structural instability, we measure the *neighbor exchange rate*, defined as the probability that a given particle changes at least one of its nearest neighbors between consecutive snapshots (corresponding to 5 seconds in experimental time)(Fig. S11).

For weak nonreciprocity ($\mathcal{N} < 1$), the system remains crystalline with minimal neighbor exchanges. Then, the neighbor exchange rate rises approximately linearly with \mathcal{N} , reflecting increasingly dynamic rearrangements. The rate eventually saturates around $\mathcal{N} \approx 1.75$, coinciding with the regime of highly transient fragments and continuous structural reorganization.

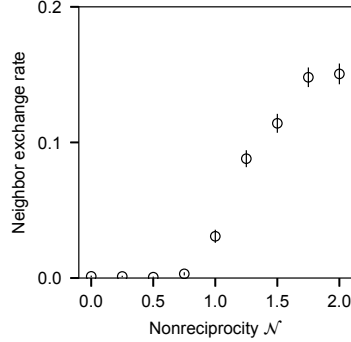


FIG. S11. **Neighbor exchanges rates as a function of nonreciprocity \mathcal{N} .** The rate remains near zero for $\mathcal{N} < 1$ and rises linearly until saturating near $\mathcal{N} \approx 1.75$.

IV. TOPOLOGICAL METRIC AND STRUCTURAL ORDER PARAMETER

A. What is a motif?

Self-organized structures are often characterized by leveraging symmetries: for example, the structure factor $S(q)$ or the pair distribution function $g(r)$ which detect translational symmetry, and the hexatic order parameter ψ_6 which measures sixfold rotational symmetry. However, many self-organized structures—as observed in the dynamic clusters of starfish embryo mixtures in their traveling state and the nonreciprocal mixture simulations with a sufficiently strong nonreciprocity $\mathcal{N} \geq 1$ —can be far away from any obvious symmetries, limiting the applicability and interpretation of conventional, symmetry-based order parameters.

To overcome this limitation, we characterize the self-organized structures via the network topology of local neighborhoods. Specifically, each particle's local neighborhood (here we choose next-to-nearest neighbors, i.e. $r = 2$) corresponds to a *topological motif*, a network in which particles are nodes and nearest-neighbor connections are edges. For example, a hexatic crystal corresponds to a topological motif with the central node (representing the focal particle) with edges to its six neighbors, whose edges connect to their subsequent neighbors (Fig. S12a).

Even for an $r = 2$ neighborhood, there are many possible motifs; we consider $\mathcal{O}(15,000)$ motifs, which are only a subset of the observed possible motifs. Although motifs do not possess intrinsic coordinates, they can be naturally quantified at the pair level: the distance between any two motifs is defined as the number of topological (T1) transitions required to transform one motif into the other (Fig. S12). This distance measure highlights the topological nature of the formalism and offers a unique connection to structural dynamics in living systems, such as tissue dynamics and morphogenesis [19].

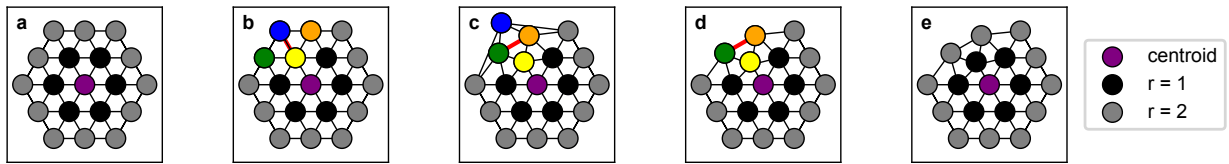


FIG. S12. Illustration of the T1 transition from the M_1 motif to the M_2 motif. (a) The hexagonal motif (M_1) has a central node (centroid) surrounded by 6 nearest neighbors ($r = 1$) and 12 next-nearest-neighbors ($r = 2$) (19 embryos total). (b)-(c) In a T1 transition, a bond flip (shown in red) occurs. During the transition, the bond between embryos which are originally nearest neighbors flips, e.g. so that the blue and yellow embryos become next-nearest-neighbors from nearest neighbors, and the green and orange embryos become nearest neighbors from next-nearest-neighbors. (d) Since a motif is comprised of embryos which are within two bonds from the centroid ($r = 2$), the blue embryo is eliminated from the motif. (e) The resulting motif is a hexagon with a 5-defect (M_2) that has 18 embryos.

B. Identification of topological motifs from data

We used the Julia topological packing statistics tool `TopologicalAnalysis` developed in [19] to extract the $r = 2$ (next-nearest-neighborhood) topological motifs and their empirical probability distributions based on embryo positions for all experiments and model simulations. Topological motifs are determined from the Delaunay triangulation of embryo positions at a single time point. Likewise, the probability of a motif corresponds to the normalized frequency of that motif at a single time point. While we do not filter triangulation edge lengths, we choose not to keep track of the motifs centered on embryos included in the convex-hull (outer envelope) of the Delaunay triangulation. Therefore, the extracted probability distributions comprise motifs centered only on embryos within the convex hull, but can include edges that connect embryos across clusters (Fig. S13).

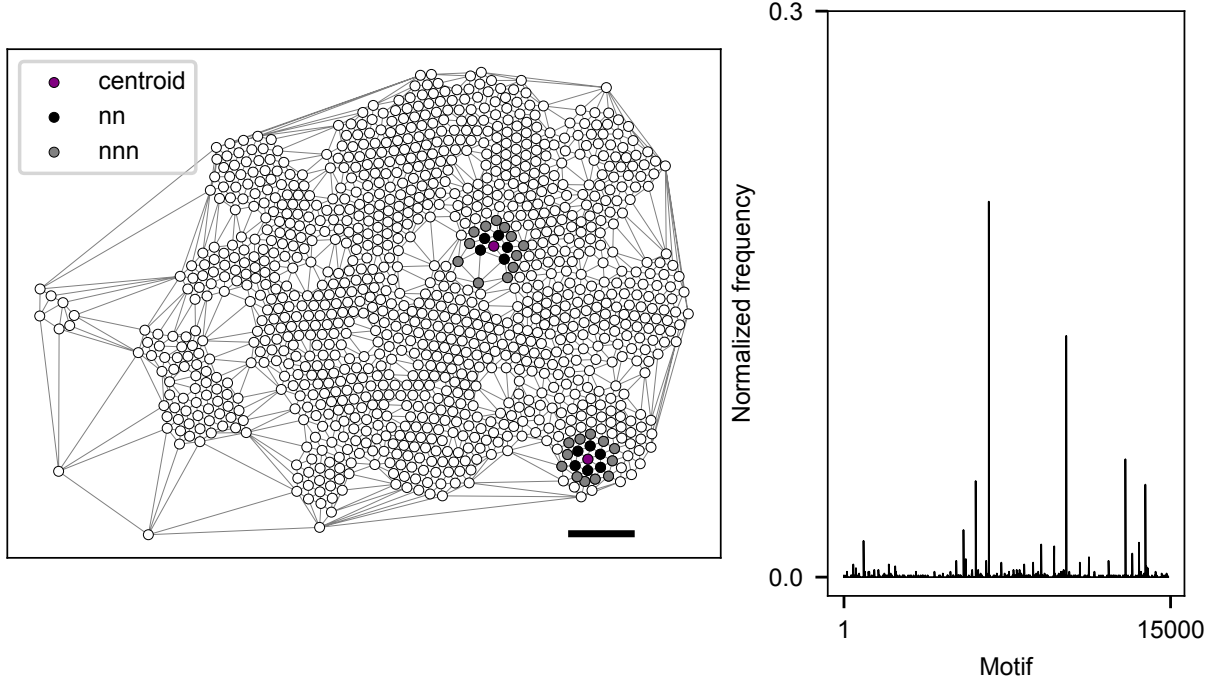


FIG. S13. **Example topological motif analysis of a configurational snapshot.** Shown here: the network of embryos at 3 hours in the mixed experiment from the main text (scale bar: $10 \mu\text{m}$). Embryo positions are triangulated using Delaunay triangulation, and motifs are extracted for the $r = 2$ (next-nearest-neighborhood) around each embryo. Two example motifs are highlighted (center: a non-hexagonal motif, bottom-right: a hexagonal motif). The centroid of each motif is depicted in purple, its nearest neighbors in black, and next-nearest-neighbors in gray. The probability distribution of all motifs from the snapshot is shown on the right.

From our inference-based model of nonreciprocal mixtures, we extract the data-driven topological flip graph [19] from the steady-states of nine representative simulations with varying nonreciprocity \mathcal{N} (from $\mathcal{N} = 0$ to 2.0 in steps of 0.25). Probability distributions are projected onto this flip graph which comprises $\mathcal{O}(15,000)$ topological motifs.

Only motifs which occurred more than ten times over the course of all simulations were incorporated into the data-driven flip graph. For all but the highest nonreciprocity values ($\mathcal{N} < 1.5$), this cutoff captured well over 80% of the motifs observed in the nonequilibrium steady-state, Table I. For the higher nonreciprocity values this cutoff reflected a lower total probability, around 65% for $\mathcal{N} = 1.5$ and half of the probability of the more diverse $\mathcal{N} = 2.0$ state. This is due to the fact that higher nonreciprocity leads to greater dynamic instability. For example, for the $\mathcal{N} = 2.0$ state, motifs observed only once in the simulation account for around 30% of its total probability. However, we find that these probability cutoffs adequately capture the diversity of the higher nonreciprocity states relative to the flocking and low reciprocity states, as evidenced by high values of $\langle d_{\text{hex}} \rangle$ and the shallower (more diverse) topological landscapes shown in the main text (Figs. 2 and 3).

Further, as shown in Section V C (Fig. S17) for $\mathcal{N} = 1$, probability drops off quickly with motif rank for the top 14 most probable motifs, indicating that a relatively small subset of the motifs are needed to capture the complexity of the $\mathcal{N} = 1$ state.

TABLE I. Total number of topological motifs observed for each of the nine representative simulations i) in the absence of a cutoff, and ii) projected onto the flip graph with a cutoff that each motif must occur greater than 10 times. For all but $\mathcal{N} \geq 1.5$, a cutoff of greater than 10 occurrences per motif captures 80% or more of the probability.

Nonreciprocity	Number of motifs (without cutoff)	Number of motifs (with cutoff)	Total probability reflected with cutoff (%)
0	71	70	99.7
0.25	159	136	99.9
0.5	37	36	99.7
0.75	386	260	99.8
1	~27,000	~2,400	90
1.25	~74,000	~3,800	80
1.5	~130,000	~4,300	65
1.75	~154,000	~4,200	60
2	~187,000	~4,200	50

C. Calculation of structural order parameter

Leveraging the motif probability distributions, p , we define the structural order parameter $\langle d_{\text{hex}} \rangle$ which describes the system-average topological distance to a hexagonal crystal:

$$\langle d_{\text{hex}} \rangle = \sum_j p(j) d_{\text{hex}}(j). \quad (17)$$

Here, j is taken to be the motif index in the flip graph, $p(j)$ is its probability, and $d_{\text{hex}}(j)$ is the topological distance between the motif and the hexagonal motif. As we will show below, this order parameter has another meaningful physical interpretation- it corresponds to the topological earth mover's distance [19] to the perfect hexagonal crystal, and thus describes the minimum cost (in units of T1 transitions) to transform the system configuration into the hexagonal crystal (SI Sec. IV A). By plotting the d_{hex} value associated with each motif for each embryo (motif centroid), we find that d_{hex} is spatially distributed throughout the crystal, with low values ($d_{\text{hex}} \leq 2$) concentrated at the center of the crystal, and higher d_{hex} values ($2 \leq d_{\text{hex}} \leq 6$) located at crystal boundaries.

Computationally, we calculate the structural order parameter $\langle d_{\text{hex}} \rangle$ by leveraging the recently developed `TopologicalAnalysis` package in Julia [19]. The topological earth mover (TEM) distance in this package is a metric to quantify the difference between two probability distributions of motifs projected onto the flip graph. It can be described as the minimum cost (in units of T1 transitions) to transform one probability distribution, p_A , into another, p_B , and is given by:

$$\text{TEM}(p_A, p_B) = \min_{\gamma} \sum_{i,j} \gamma_{ij} d(i, j), \quad (18)$$

where γ corresponds to a transport map between the distributions that satisfies $\sum_j \gamma_{ij} = p_A(i)$ and $\sum_i \gamma_{ij} = p_B(j)$ with $\gamma_{ij} \geq 0$. Here, $d(i, j)$ denotes the topological distance (number of connecting edges) between two motifs on the flip graph.¹

In the case where one of the probability distributions contains a single motif, e.g.:

$$p_A(i) = p_{\text{hex}}(i) = \begin{cases} 1 & \text{if } i = \text{index for hexagonal motif} \\ 0 & \text{else,} \end{cases} \quad (19)$$

¹ Note that the TEM distance can take on any value greater than or equal to zero, while the topological distances $d(i, j)$ are constrained to nonnegative integers.

then the TEM distance given in Eq. (18) reduces to $\langle d_{\text{hex}} \rangle$, a weighted average of the distances $d_{\text{hex}}(j) = d(\text{hex}, j)$ of the motifs present in distribution p_B from that single motif (the hexagon). That is,

$$\langle d_{\text{hex}} \rangle = \sum_j p_B(j) d_{\text{hex}}(j) = \text{TEM}(p_{\text{hex}}, p_B) = \min_{\gamma} \sum_{i,j} \gamma_{ij} d(i, j). \quad (20)$$

This follows from the fact that there is only one way to minimally transform the single motif distribution, p_{hex} , into any other distribution p_B : $\gamma_{\text{hex},j} = p_B(j)$.²

As further evidence that $\langle d_{\text{hex}} \rangle$ is the relevant structural order parameter, we perform a clustering analysis on the TEM distance matrix between the nine representative simulations for the nine different nonreciprocity values (Fig. S14). The matrix shows two distinct clusters for low nonreciprocity values ($\mathcal{N} < 1$) and high nonreciprocity values ($\mathcal{N} > 1$), separated by the $\mathcal{N} = 1$ state. A two-dimensional embedding of the TEM distance matrix performed using multidimensional scaling (MDS) further delineates these clusters (Fig. S14). In particular, the first principal component of the MDS embedding scales linearly with the TEM distance to hexagon ($\langle d_{\text{hex}} \rangle$).

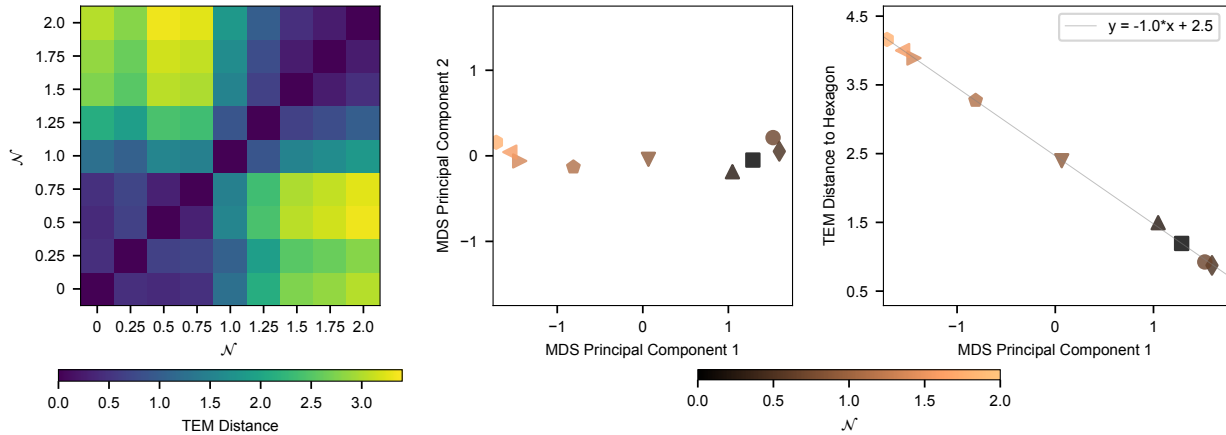


FIG. S14. **TEM distance matrix between simulations clusters based on nonreciprocity.** Left: TEM distance between the nine representative simulations used to determine the data-driven flip graph. There are distinct clusters that distinguish low nonreciprocity values ($\mathcal{N} < 1$) from higher nonreciprocity values ($\mathcal{N} > 1$), with $\mathcal{N} = 1$ acting as a boundary between these clusters. Right: A two-dimensional embedding of the TEM distance matrix using classical multidimensional scaling. The first principal component corresponds to the TEM distance to the hexagon (line of best fit shown in gray).

D. Nonreciprocal self-healing

Our interaction inference reveals that E1 and E2 embryos experience distinct self-interactions (SI Sec. II A). Consequently, even in the reciprocal case ($\mathcal{N} = 0$), model simulations produce a bi-disperse crystal containing a finite fraction of defects.

Surprisingly, introducing a weak nonreciprocity enhances crystalline order. This effect, captured in the main text via our topological metric, is corroborated here by both the reduction of 5- and 7-fold defects and the enhancement of the hexatic order $\langle |\psi_6| \rangle$ (Fig. S15). This *nonreciprocal self-healing* is counterintuitive, given that nonreciprocity is known to promote instabilities and dynamics.

² Consider the simple test case $p_A = [1, 0, 0]$ and $p_B = [0.7, 0.1, 0.2]$ where we find that $\gamma = ((0.7, 0.1, 0.2), (0, 0, 0), (0, 0, 0)) = (\vec{p}_B, \vec{0}, \vec{0})$.

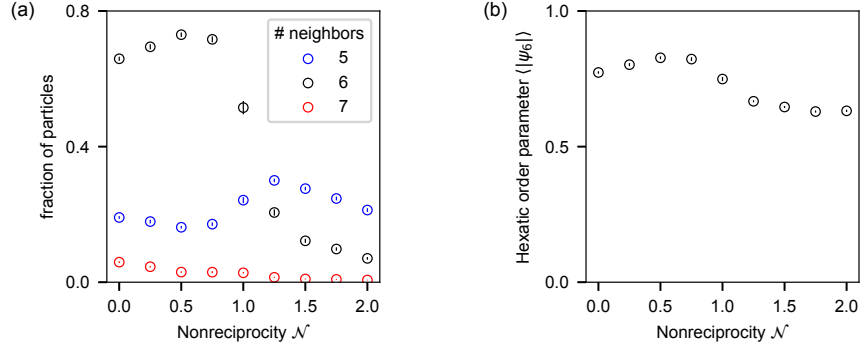


FIG. S15. Number of defect supports nonreciprocal self-healing. (a) Weak nonreciprocity ($\mathcal{N} < 1$) reduces the number of 5- and 7-fold defects, driving the system toward a more ordered crystal. (b) The same regime enhances the hexatic order $\langle |\psi_6| \rangle$, indicating improved crystalline order.

We interpret this effect as analogous to annealing. Nonreciprocity introduces local stresses that destabilize low-symmetry or weakly ordered regions, while highly symmetric crystalline neighborhoods remain robust. As these defective regions reorganize, the system approaches a near-perfect crystal. Stronger nonreciprocity, in contrast, can destabilize even high-symmetry structures and promotes cluster breakage.

This selective stabilization is reminiscent of order-by-disorder phenomena and dissipative engineering, where low-symmetry configurations may be preferentially removed to enhance overall order. A quantitative understanding of this mechanism, particularly how collective effects from particles outside the local neighborhood contribute to self-healing, remains an interesting direction for future work.

V. TOPOLOGICAL LANDSCAPE

We take advantage of the topological metric space of the flip graph (SI Sec. IV) to elucidate underlying differences in the spread across motif compositions of the probability distributions, by constructing topological landscapes.

A. Defining a low-dimensional manifold from topological flipgraph via multidimensional scaling

We compute a two-dimensional embedding of the metric space using multidimensional scaling (MDS) [20] that forms the foundation (xy plane) for all our landscapes. Here, each motif j corresponds to a single point (x_j, y_j) in the foundation. The height z_j in the landscape is given by the observed motif probability $p(j)$. We use classical MDS on the pairwise distance matrix D (with $D_{ij} = d(i, j)$) between topological motifs, determined from their graph distances. This two-dimensional embedding method is chosen to best preserve pairwise distances [20] and serves our purpose of data visualization.

On average, increasing distances in the flip graph correspond to increasing distances in the embedded space and follow a monotonic trend (Fig. S16).

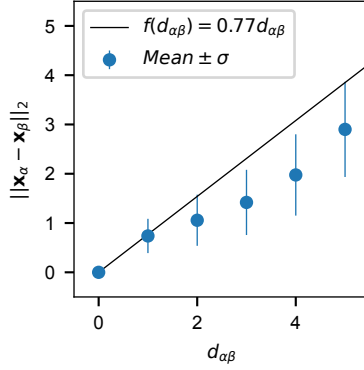


FIG. S16. **Larger flip graph distances correlate with larger distances in the MDS embedding.** Shepard plot comparing the pairwise distances between motifs in the MDS embedded space, $\|x_i - x_j\|_2$, to the true distances, d_{ij} , on the flip graph for the 2-dimensional embedding. On average, larger distances in the MDS space correspond to larger distances on the flip graph, and this trend is monotonic. Errorbars correspond to one standard deviation from the mean.

B. Mapping frequency of motifs to probabilities on the manifold via kernel density estimation

To transform the discrete probability landscape into a smooth landscape, we use kernel density estimation [21]. At each motif coordinate, we place a Gaussian kernel, weighted by its observed probability. The estimator for the density is given by:

$$\hat{f}_b(x, y) = \frac{1}{N} \sum_{j=1}^N K_b(x - x_j, y - y_j) = \frac{1}{N} \sum_{j=1}^N p(j) \exp\left(-\frac{r(j)^2}{b^2}\right), \quad (21)$$

where $p(j)$ is the probability of motif j ($j \in [1, N]$), $r(j) = \sqrt{(x - x_j)^2 + (y - y_j)^2}$, and b is the smoothing bandwidth. Adapting the rule of thumb by Bowman and Azzalini [21], we use the following bandwidth for the Gaussian kernel:

$$b = \left(\frac{4}{N(d+2)}\right)^{1/(d+4)} \frac{\tilde{\sigma}}{0.6745} \quad (22)$$

The term $\tilde{\sigma}$ is the mean absolute deviation estimator, which here we approximate by $\tilde{\sigma} = \sqrt{\left(\overline{|x_j - \bar{x}_j|}\right)^2 + \left(\overline{|y_j - \bar{y}_j|}\right)^2}$ where $\overline{(\cdot)}$ represents the mean with respect to the MDS data (the motifs).

Kernel density estimates were computed on grids with a resolution much lower than the average distance between points (128×128 grid with x and y each ranging from [-4,4] for a bin size of 0.0625×0.0625). For 1-dimensional landscapes along M_1 - M_2 axis, all probability distributions are discretized with a bin size of 0.0101, corresponding to 1% of the M_1 - M_2 distance.

C. Atlas of topological motifs in simulation and experiment

In the main text, we show the 14 motifs that have frequency over 1% in simulations with $\mathcal{N} = 1$. Here we show the same motif atlas with full labels on the low-dimensional manifold (Fig. S17a).

In addition, we show the 14 most-observed motifs in the experiment (Fig. S17b). We label these top 14 motifs as M_1 to M_{14} in the order of decreasing frequencies. Notably, the top 6 motifs are identical to the top 6 motifs observed in the simulation with $\mathcal{N} = 1$; thus M_1 and M_2 found in $\mathcal{N} = 1$ are consistent with the top two motifs defined based on the frequency in the experiment.

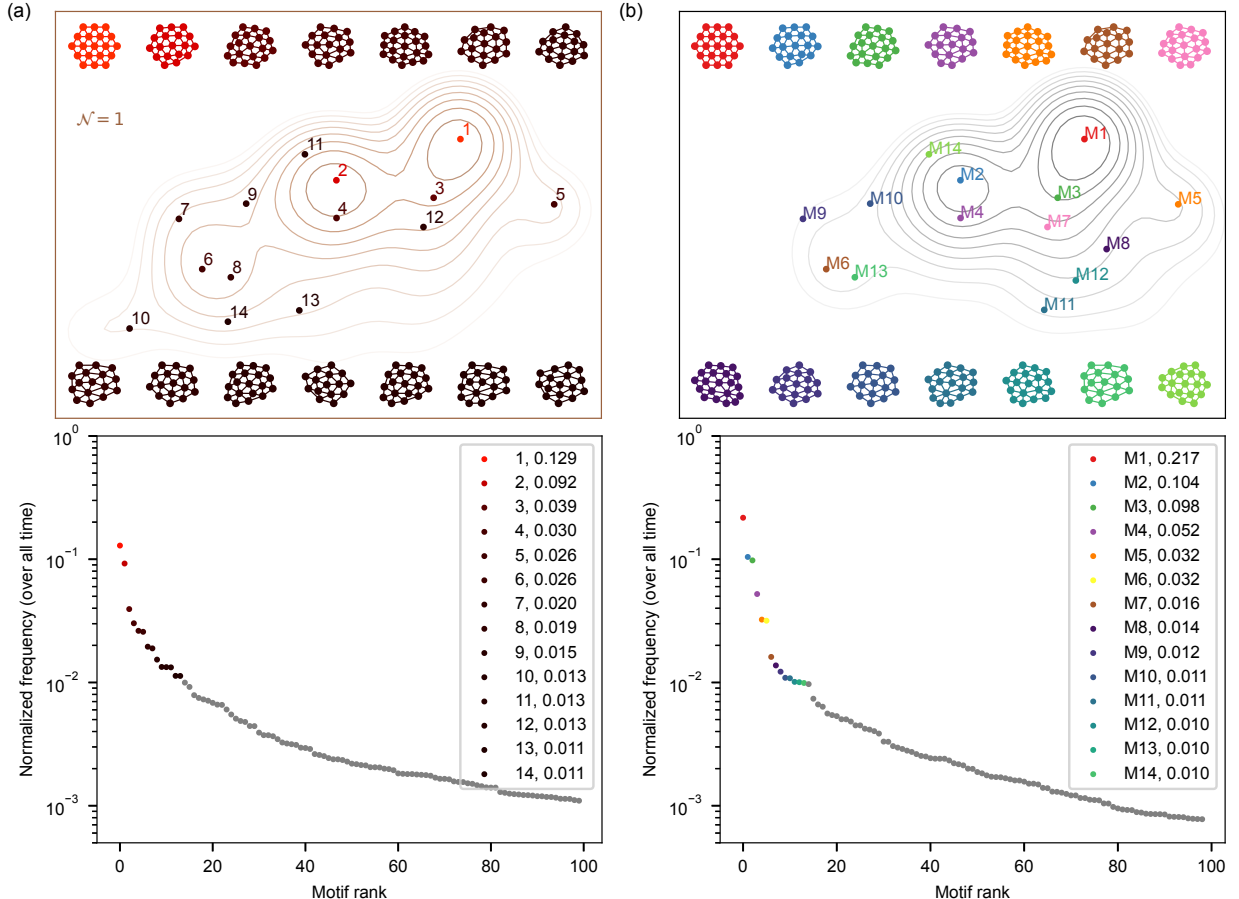


FIG. S17. **Atlas of topological motifs from simulation and experiment** (a) *Top*: Atlas of motifs from simulation with inferred nonreciprocity $\mathcal{N} = 1$. This contains identical information with Fig. 3c, but is enlarged with labels up to the 14th most observed motif. *Bottom*: Normalized motif frequencies over all time in model with $\mathcal{N} = 1$. (b) *Top*: Atlas of motifs from experiment. Motifs up to M_6 (6th most observed motif) are identical to A. *Bottom*: Normalized motif frequencies over all time in experiment.

D. Spatiotemporal distributions of topological motifs M_1 and M_2

M_1 and M_2 are the two most dominant topological motifs in both experiment and simulation with experimentally inferred $\mathcal{N} = 1$. Characterizing their spatial distributions may provide insight into how local structure relates to global organization in nonreciprocal mixtures.

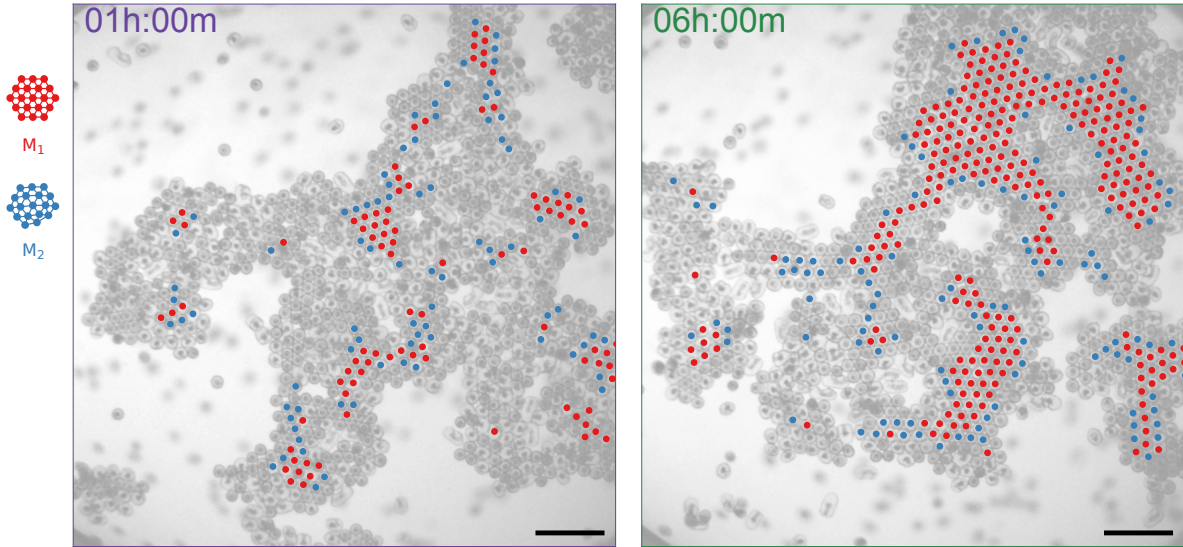


FIG. S18. Spatial distributions of topological motifs M_1 and M_2 . M_1 , a perfect crystal, is labeled as red, while M_2 , an almost-perfect crystal with a 5-fold defect, is labeled as blue. Compared to early time, the late-time snapshot from the experiment shows many more M_1 motifs.

As shown in Fig. S18, M_1 motifs are primarily located in the crystalline cores of clusters, whereas M_2 motifs appear preferentially at their peripheries. Consequently, the relative abundance of these motifs reflects the system's global organization: large, well-ordered crystals are dominated by M_1 , while fragmented or loosely packed configurations exhibit an increased fraction of M_2 .

In addition to the spatial distribution, we also elucidate here how the frequencies of M_1 and M_2 motifs change over time. Over time, M_1 increases in its proportion in the experiment while the frequency of M_2 stays constant (Fig. S19).

E. Transition between M_1 and M_2 in experiment is indirect

In the main text, we find that the structural transition near nonreciprocity $\mathcal{N} = 1$ is a first-order-like transition that involves a coexistence state between M_1 and M_2 . Since many features of phase transitions only become meaningful in thermodynamic limit, this analogy between the nonreciprocal transition in structure and first-order phase transitions does not imply that the nonreciprocal transition *is* a first-order phase transition. Instead, by connecting the complex biological system to a well-established theoretical framework, the analogy opens new avenues of testable predictions. Here, we will demonstrate one example of these predictions and its validation.

The coexistence state of M_1 and M_2 imply that the two configurations are separated by a set of configurations that are less likely than either. While the two motifs are in fact apart by a single T1 transition, we find that the transition between two motifs is more often indirect (mediated by other motifs) than direct (Fig. S20a). In particular, despite its lower frequency, M_3 exchanges significant probability flux with both M_1 and M_2 that is comparable to the direct flux between M_1 and M_2 .

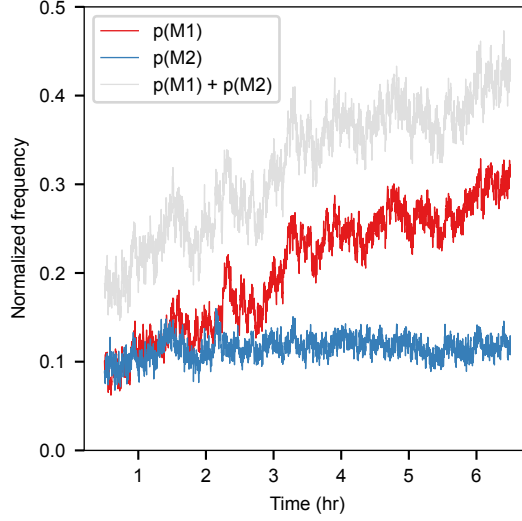


FIG. S19. **Probability of M_1 and M_2 motifs over time in main experiment.** The transition at ~ 3 hr coincides with an increase in the probability of M_1 .

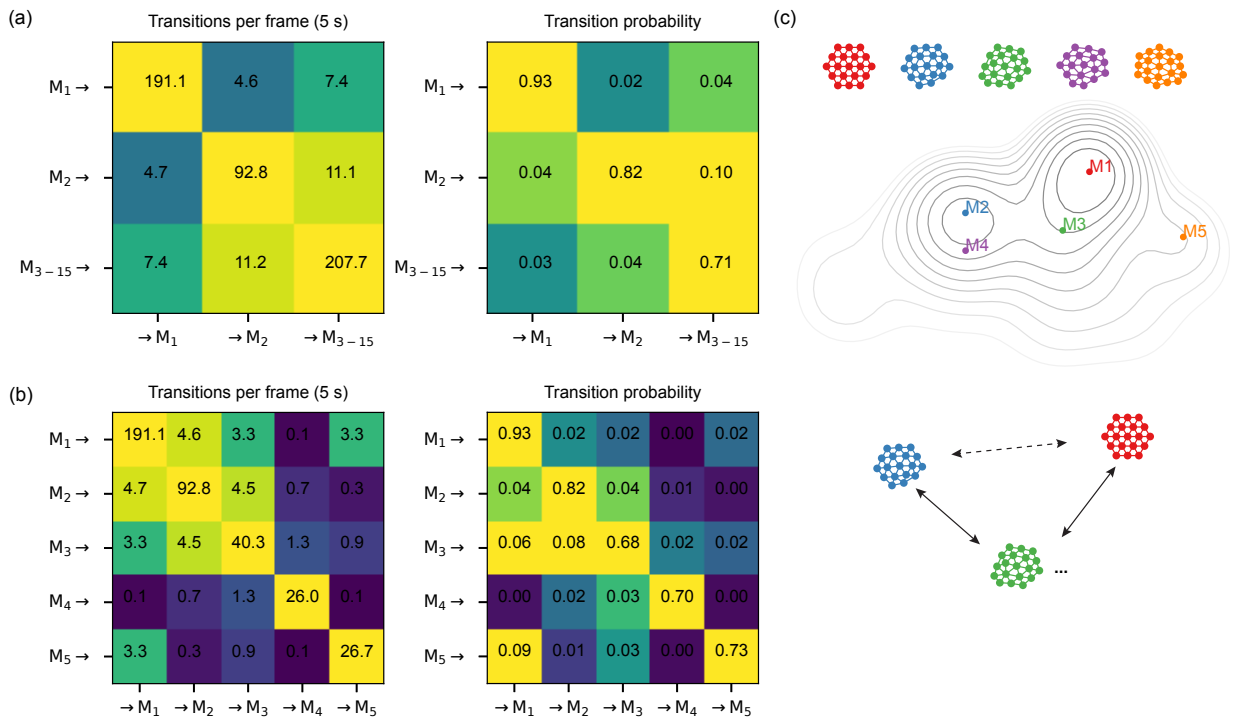


FIG. S20. **Transition between M_1 and M_2 in experiment is indirect.** (a) Transition between M_1 and M_2 is often mediated by other motifs, even though the direct transition is allowed. (b) M_3 and M_5 are major intermediate motifs that mediate the transition between M_1 and M_2 . (c) Top: Shapes of motifs M_1 - M_5 and their locations in low-dimensional manifold. Bottom: A cartoon of transition between motifs.

VI. TOPOLOGICAL FLOWSCAPE

Before presenting the technical details of our flowscape construction (SI Sec. 6.2), we first outline the general concept of a *flowscape*, which is broadly applicable to any series of probability landscapes.

We introduce the flowscape as a framework for visualizing the temporal evolution of high-dimensional structural configurations in a reduced and interpretable space. Specifically, we consider a time series of probability distributions $P(X; t)$ defined over a discrete set of states x_i , with corresponding probabilities $p_i(t) \equiv P(x_i; t)$, satisfying $\sum_i p_i(t) = 1$. In the main text (Fig. 4), x_i corresponds to coordinates in a coarse-grained, low-dimensional manifold constructed from topological motif distributions (topological landscapes), and t denotes experimental time. The flowscape embeds these evolving distributions into a reference-based information space, enabling intuitive visualization of time-dependent landscapes.

To define the flowscape, we select one or more reference distributions $\{Q^a(X)\}$, each represented as a discrete probability vector $\{q_i^a\}$. These references may correspond to canonical structural states (e.g., M_1 -like, M_2 -like, initial state, or final state), serving as anchors against which the current system state is compared.

For each time point t , we compute the Kullback-Leibler (KL) divergence from the instantaneous distribution $P(t)$ to each reference Q^a :

$$D_{\text{KL}}(P(t) \| Q^a) = \sum_i p_i(t) \log \left(\frac{p_i(t)}{q_i^a} \right) \quad (23)$$

We then use the KL divergence from each reference to create an embedding of each distribution $P(t)$ as a point in \mathbb{R}^n , where n is the number of reference states. For instance, in Fig. 4c of the main text, we embed the evolving state as a trajectory in a 2D space defined by divergences to two reference distributions. Each coordinate quantifies how structurally dissimilar the current state is from a corresponding reference. In this paper, since P —the landscape of topological motifs—represents a state of self-organized structure, each flowscape point reflects the instantaneous structural dissimilarity from designated reference structural state.

A. Conceptual basis of the flowscape

Before addressing the specific construction of the topological flowscape used in our system, we discuss general features of the framework that apply to any evolving probability distribution.

a. Choice of divergence metric. We primarily use Kullback-Leibler (KL) divergence due to its interpretability and strong foundation in information theory. However, the conceptual framework of the flowscape does not depend on this specific choice. Alternative measures, including the symmetric Jensen-Shannon divergence and Wasserstein (earth mover’s) distance, can also be used, each with different sensitivities to distributional changes. For instance, in SI Sec. VII C, we construct a variant of the flowscape using the topological earth mover (TEM) distance.

b. KL asymmetry and interpretation. KL divergence is not symmetric, i.e., $D_{\text{KL}}(P \| Q) \neq D_{\text{KL}}(Q \| P)$. In our case, the references correspond to well-defined structural states, and the KL divergence measures how much information is “lost” when approximating the current state with that reference.

c. Flowscape and information geometry. Flowscapes do not explicitly encode information flow or entropy production, as they are constructed solely from snapshots of probability distributions without requiring transition rates. Nevertheless, KL divergences can bound or approximate informational quantities, drawing conceptual parallels to results in information geometry and stochastic thermodynamics. These connections suggest that flowscape trajectories may carry latent thermodynamic structure, even when derived from static distributions. In SI Sec. VII B, we illustrate this link by analyzing information rate transitions, demonstrating how flowscapes can reflect underlying dynamical constraints.

B. Details of topological flowscape introduced in the main text

In Fig. 4c of the main text, we construct a flowscape using two reference distributions chosen to highlight the transition between the self-organized states. Specifically, the references are defined as one-dimensional Gaussian distributions along the M_1 – M_2 axis:

$$Q^x = \text{Normal}(M_2, \sigma), \quad Q^y = \text{Normal}(M_1, \sigma),$$

where the 1-dimensional time-dependent distributions $P(t)$ are taken from Fig. 4b. The width σ of each reference is set to the time-averaged kernel width of the experimental landscape, obtained via Eq. (22).

This construction reflects a stepwise simplification of the complex structural landscape toward an interpretable representation. While a flowscape could, in principle, be constructed using two-dimensional distributions over the low-dimensional manifold—or even higher—dimensional distributions retaining additional manifold directions, our 1D construction specifically emphasizes transitions along the M_1 – M_2 axis, primarily visualizing transitions between these two structural states with less emphasis on dynamics far from this axis.

For the KL divergence calculation, all probability distributions are discretized with a bin size of 0.0101 in the low-dimensional coordinate, corresponding to 1% of the M_1 – M_2 distance. The reference width $\sigma = 0.0606$ matches the kernel width of the experimental landscape. All distributions are normalized to satisfy $\sum_i p_i = 1$, and the flowscape coordinates (KL divergences) are then evaluated using Eq. (23).

C. Flowscape of inference-based model over the change in nonreciprocity

Our flowscape in the main text uses topological landscapes from experiment over time. Here, we show flowscape of topological landscapes from model simulations over nonreciprocity \mathcal{N} .

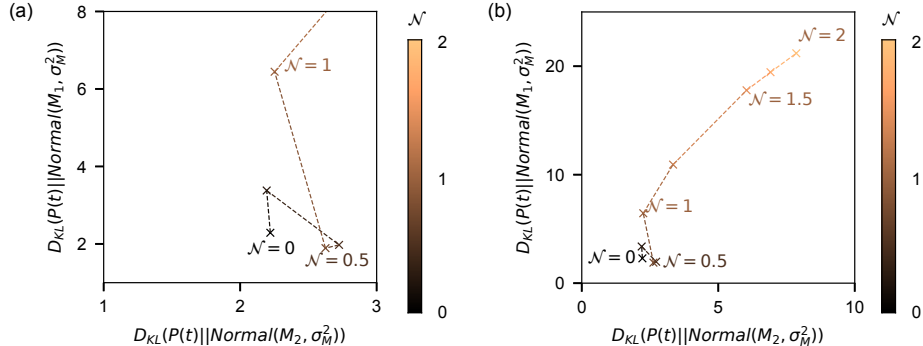


FIG. S21. Flowscape of inference-based model over the change in nonreciprocity. (a) Flowscape of inference-based model, with the same x- and y- axes ranges as in the main text Fig. 4c. The trajectory passes through the lower-right corner unlike the experimental flowscape, as the intermediate $\mathcal{N} = \{0.5, 0.75\}$ bring the system closest to a perfect crystal. (b) The same flowscape with larger ranges of x- and y- axes. As nonreciprocity exceeds $\mathcal{N} = 1$, the system moves away from both M_1 and M_2 .

The flowscape of the inference-based model recapitulates how nonreciprocity leads to different self-organized structures (Fig. S21). First, at weak nonreciprocity $\mathcal{N} < 1$, the trajectory traverses into the lower-right corner of the flowscape where it is closest to M_1 , as nonreciprocity anneals the crystal and removes defects (Fig. S21a). Second, at strong nonreciprocity $\mathcal{N} > 1$, the trajectory moves away from both axes, indicating a strong deviation from a crystalline structure as the system becomes more fragmented (Fig. S21b).

D. Characterization of the transition state

Unlike the flowscape of model simulations where \mathcal{N} is varied, the experimental flowscape reveals a transition trajectory from $\mathcal{N} = 1$ to $\mathcal{N} = 0$ that passes through states located in the lower-left corner of the flowscape, near both M_1 and M_2 . These “transition states” do not correspond to a steady state in model simulations under fixed \mathcal{N} .

Inspection of the topological landscape at the transition (e.g., Frame 2210) shows the emergence of a third peak at M_5 , corresponding to a motif containing a 7-fold defect (Fig. S22). The spatial distribution of motifs further reveals that M_2 (5-defect), M_4 (5-7 defect pair), and M_5 (7-defect) form extended lines of defects as the embryo mixture transitions from the traveling to the fluctuating state. Consistently, the frequencies of M_4 and M_5 peak at intermediate times, whereas other motifs, such as M_6 , do not follow this trend.

Based on these observations, we interpret the transition state as a *hollow crystal*. During the transition, multiple clusters merge gradually rather than instantaneously. When two clusters meet, they initially leave an empty void between them, which fills only slowly over time. This contrasts with the model simulations, where steady states either form a nearly perfect crystal or exhibit zipper-like fractures and continuous line mergers, but do not produce hollow clusters.

E. Motif cycles in cluster merging and fragmentations

In the main text Fig. 4d, we show that flowscape admits a versatile choice of reference states. In particular, by taking experimental snapshots from different timepoints as references, we can use flowscape as a temporal microscope that can zoom into small-scale, rapid changes in structures.

In our experiment, this fine signature turns out to represent repeated cluster merging and fragmentation. Here, we elaborate on this observation by focusing on a particular cycle in the flowscape with a short (30 minutes) time gap between references (Fig. S23). From experimental snapshots, we find that the cycle corresponds to a merger-and-breaking of multiple clusters, which accompanies the closing-and-opening of gaps between them (Fig. S23a). The time series of frequencies of individual motifs offers a detailed view of this phenomenon, marked by the peak of the crystalline M_1 motif probability at the middle of the cycle (Fig. S23b).

This time series of motifs reveals interesting interactions between structures (Fig. S23c). Specifically, the chirality of trajectories in M_1 - M_2 space and M_1 - M_3 space suggests that an increase in M_2 follows an increase in M_1 , while an increase in M_3 precedes an increase in M_1 . This cyclic relation also connects to an emergent nonreciprocity: high probability of M_1 leads to an increase in M_2 , while high probability of M_2 accompanies a decrease in M_1 . Understanding these intricate nonequilibrium dynamics between the topological motifs could be an interesting future direction to follow.

F. Topological flowscape of additional experiments

Here, we apply our conceptual toolbox—topological landscape and topological flowscape—to additional experiments described in SI Sec. ID, which exhibited two distinct states: a demixed LCC and an orbiting mixture.

1. Demixed LCC

In the demixed LCC experiment where E2 embryos swim to the air-water interface before E1 embryos, the self-organized structure remained almost crystalline. This is recapitulated in Fig. S24a: the peak at the crystalline motif M_1 remains in the topological landscapes over time. Nevertheless, Fig. S24b suggests that the structure is still dynamic over time. The landscape slices along M_1 - M_2 axis reveal that, while M_1

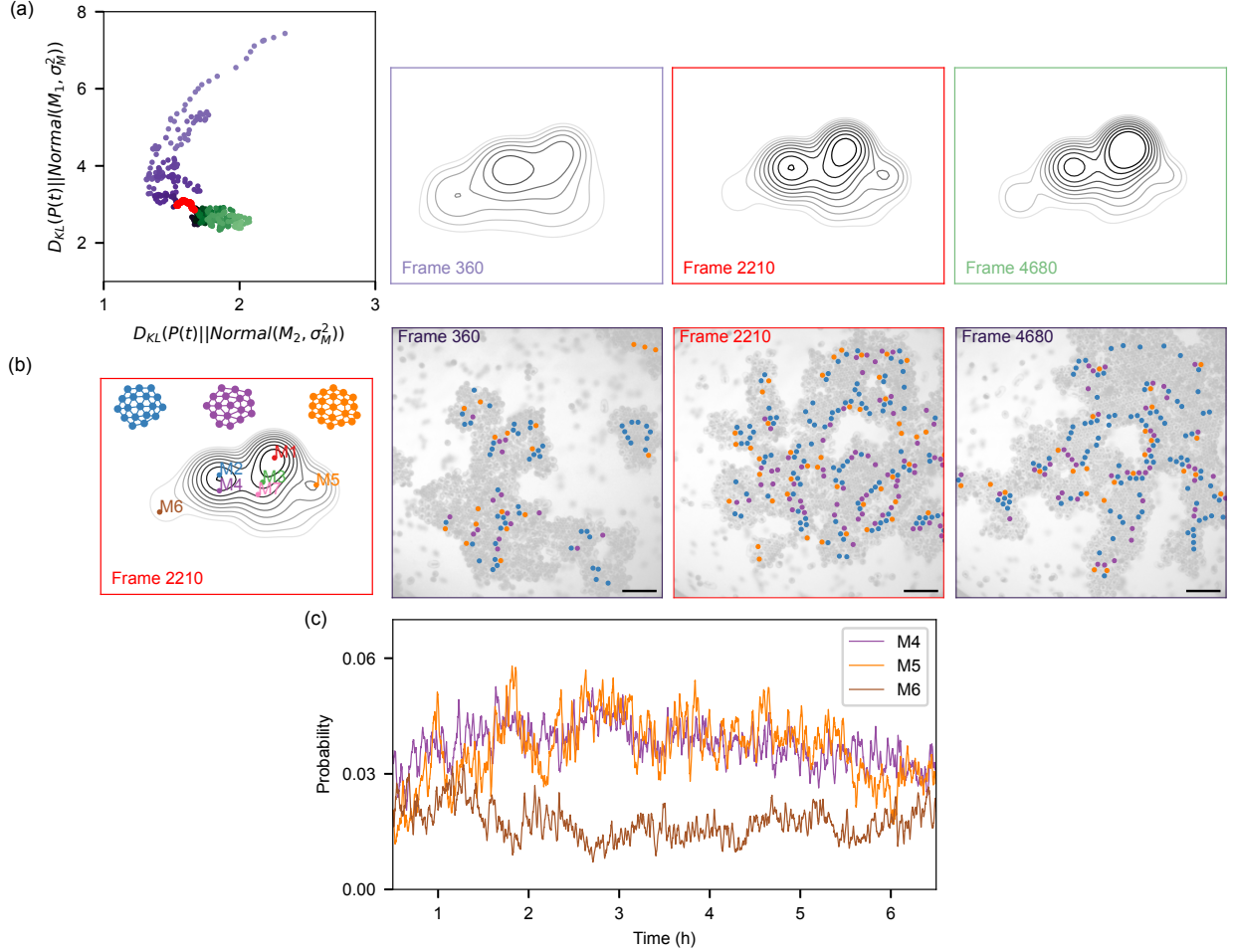


FIG. S22. **Traveling-fluctuating transition proceeds through hollow crystals.** (a) Flowscape trajectory indicates that the transition between $\mathcal{N} = 1$ -like and $\mathcal{N} = 0$ -like regimes passes through a distinct intermediate state around Frame 2210 (~ 3 h), marked by the appearance of a third peak. (b) This peak corresponds to motif M_5 , which contains a 7-fold defect and whose frequency maximizes at the transition. Motifs M_2 (5-defect), M_4 (5–7 defect pair), and M_5 (7-defect) organize into defect lines surrounding voids, producing a hollow crystal not observed in simulations. (c) The frequencies of M_4 and M_5 peak at intermediate times, whereas other motifs, such as M_6 , do not follow this trend.

remains the most dominant peak, the M_2 peak grows and shrinks over time.

The flowscape in Fig. S24c resolves the structural dynamics over time. At first, the system quickly develops a crystalline structure, approaching M_1 . At around 16 hours, the system drifts away from M_1 and towards M_2 , followed by a re-entrance towards M_1 and away from M_2 . We find that a large-scale crystal rearrangement occurs at this time (16 hours), in which the system almost divides into two crystals and then merges back together. This highlights that this demixed LCC regime still exhibits distinct dynamics from a homogeneous LCC that was previously reported [5].

2. Orbiting mixture

In the orbiting mixture experiment where the embryos form a boundary-filling crystal, the structure remains mostly crystalline but with significant internal rearrangements. This is recapitulated in Fig. S25a: while the peak occurs at the crystalline motif M_1 in the topological landscapes, a third peak other than M_2 emerges

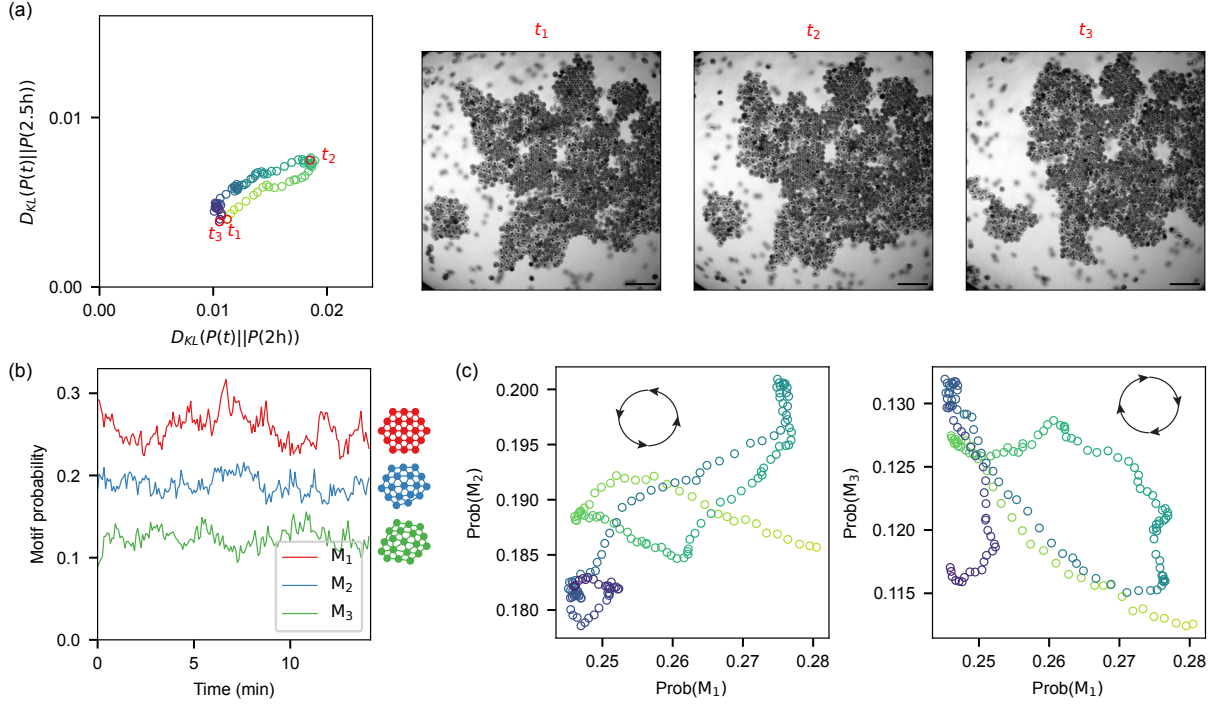


FIG. S23. **Motif cycles in cluster merging and fragmentation.** (a) *Left*: a portion of the flowscape shown in main Fig. 4d, focusing on a single cycle. *Right*: Snapshot images of experiment at early, middle, and late points of the cycle. (b) Time series of probabilities of three dominant motifs M_1 , M_2 , and M_3 . Shapes of the motifs are shown at the right side of the time series. (c) Trajectory of the probabilities shown in b, averaged over 3-minute time windows.

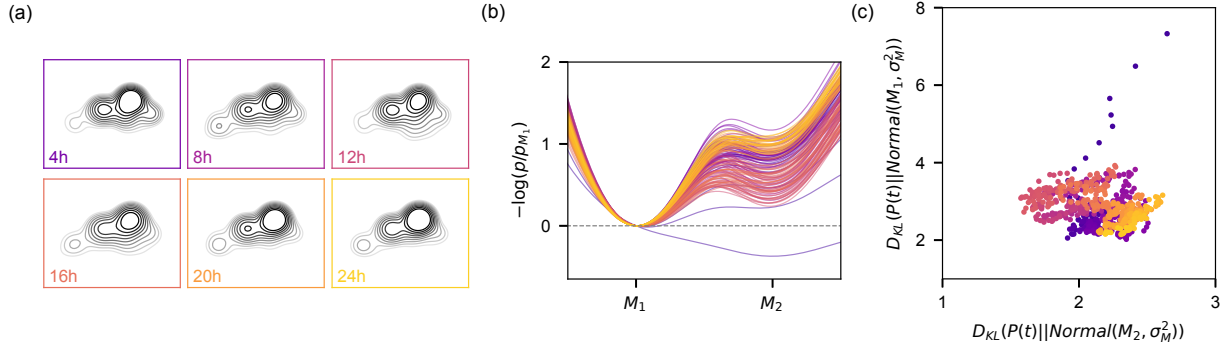


FIG. S24. **Topological landscape and flowscape of a demixed E1-E2 mixture experiment.** (a) Topological landscapes of the demixed experiment over time (b) M_1 - M_2 slice of topological landscapes over time. (c) Topological flowscape. The system exits the crystalline state at 16h, followed by a reentrance.

at the lower-right regime of the M_1 peak. This third peak corresponds to a topological motif M_5 that is extensively discussed in SI Sec. VID. This M_5 -peak emerges from the presence of holes in the crystalline structure, which are surrounded by M_5 and other defect-containing motifs.

In Fig. S25b, landscape slices along the M_1 - M_2 axis exhibit a transition that is also first-order-like through M_1 - M_2 coexistence. However, in contrast to the main experiment, the M_2 -dominance is short-lived as M_1 starts to dominate over M_2 within the first 30 minutes in the experiment.

These structural dynamics are represented on a flowscape (Fig. S25c). We find a rapid initial descent and turn, like in our main experiment. Later, the system shows an interesting oscillation over a same short line segment on the flowscape, over which M_1 increases while M_2 decreases (and vice versa).

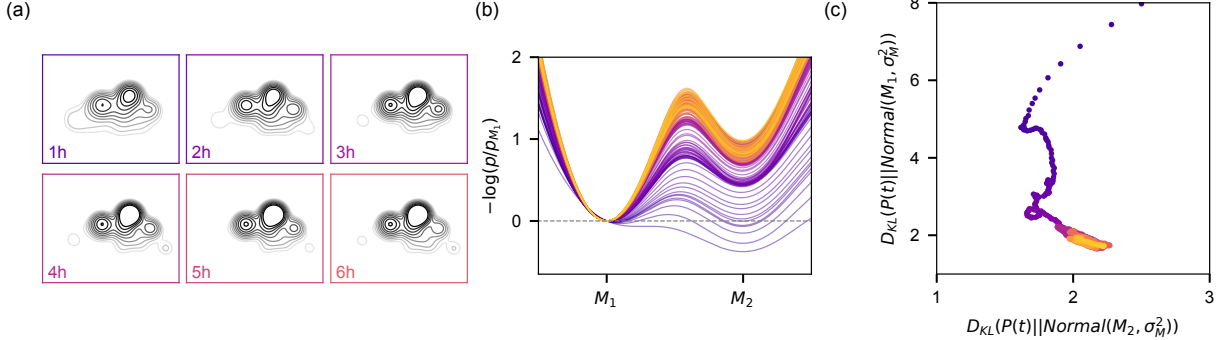


FIG. S25. **Topological landscape and flowscape of an orbiting E1-E2 mixture experiment** (a) Topological landscapes of the experiment over time. There is a pronounced third peak at M_5 , which contains a single seven-fold defect. (b) M_1 - M_2 slice of topological landscapes over time. (c) Topological flowscape of the experiment over time.

VII. ADDITIONAL ANALYSIS

A. Estimation of entropy production rate

We observe that the flowscape of the main experiment exhibits a rate transition coinciding with the macroscopic transition in velocity polarization. To further quantify this synchrony, we sought an information-theoretic rate estimate that does not rely on the sequential dimensional reduction of the topological landscape and flowscape framework. We achieve this by applying a well-known speed limit for stochastic processes.

Shiraishi et al. [22] derived a speed limit for classical stochastic Markov processes using the Hatano–Sasa entropy production [23], which remains valid for nonequilibrium dynamics with finite stationary currents:

$$\tau \geq \frac{c^* L(\mathbf{p}(0), \mathbf{p}(\tau))^2}{2 \Sigma_{HS} \langle A \rangle_\tau}. \quad (24)$$

The timescale τ sets a speed limit for a transition between two probability distributions $\mathbf{p}(0)$ and $\mathbf{p}(\tau)$ from different times $t = 0$ and $t = \tau$, with the net Hatano–Sasa entropy production Σ_{HS} and the time-averaged activity $\langle A \rangle \equiv \frac{1}{\tau} \int_0^\tau dt \sum_{i \neq j} W_{ij}(t) p_j(t)$. Here, $c^* = 0.896\dots$ is a numerical constant and $L(\mathbf{p}(0), \mathbf{p}(\tau)) \equiv \sum_i |p_i(0) - p_i(\tau)|$ is the statistical distance with the L^1 norm.

By rearranging this relation, we obtain a lower bound for the Hatano–Sasa entropy production over the time interval τ :

$$\Sigma_{HS} \geq \frac{c^* L(\mathbf{p}(0), \mathbf{p}(\tau))^2}{2 \langle A \rangle_\tau \tau}. \quad (25)$$

Because the Hatano–Sasa entropy production bounds the total entropy production from below, this provides a conservative estimate of the entropy production rate.

We used the full motif probability vector \mathbf{p} (length $\sim 15,000$) with a time gap $\tau = 20$ s (4 frames) to compute the statistical distance $L(\mathbf{p}(t), \mathbf{p}(t + \tau))$ and activity $\langle A(t) \rangle_\tau$ over time, and used Eq. (25) to estimate the Hatano–Sasa entropy production bound Σ_{HS} . Importantly, this procedure relies solely on motif frequencies to calculate $\mathbf{p}(t)$ and the activity $\langle A(t) \rangle_\tau$, derived from the transition rates $W_{ij}(t)$ between motifs; it does not require constructing the topological landscape or flowscape.

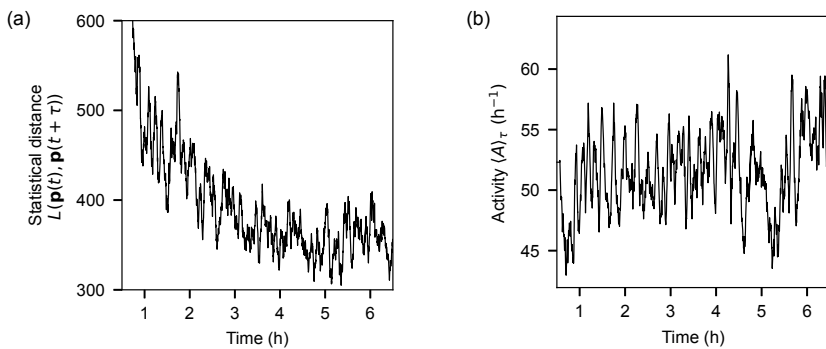


FIG. S26. **Statistical distance and activity over time.** (a) Statistical distance $L(\mathbf{p}(t), \mathbf{p}(t + \tau))$ with $\tau = 20$ s, computed using the L^1 norm. (b) Time-averaged activity $\langle A(t) \rangle_\tau = \frac{1}{\tau} \int_0^\tau dt' \sum_{i \neq j} W_{ij}(t + d\tau') p_j(t + d\tau')$. The combination of the activity and statistical distance yields a lower bound on the Hatano–Sasa entropy production rate.

Fig. S26 shows the two components required to estimate the entropy production rate (EPR): statistical distance and activity. The EPR transition, shown in Fig. 4f of the main text, is primarily driven by the statistical distance, while the activity remains relatively constant over time.

B. Information rate over time exhibits a rate transition

In addition to KL divergence-based distinguishability and an independent entropy production rate estimate, here we present yet another quantification of an information rate which is based on information geometry.

Specifically, for the main experiment, we calculate the information rate:

$$\Gamma(t) \equiv \sqrt{\frac{2}{dt} J(p(x, t + dt) | p(x, t))}. \quad (26)$$

with timestep $dt = 5$ s and Jensen-Shannon Divergence $J(P|Q) \equiv \frac{1}{2}(D_{KL}(P|Q) + D_{KL}(Q|P))$.

In Fig. S27, we find that the information rate both slows down and fluctuates less at around 3 hours, the time of traveling-fluctuating transition. This reinforces our observation that an information rate shift accompanies the state transition in the main experiment (Fig. 4f, Fig. S26). Moreover, the suppression of fluctuation offers an additional informational signature that could be investigated in future work.

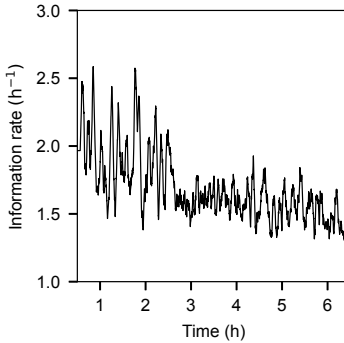


FIG. S27. Information rate $\Gamma(t)$ (based on the Jensen-Shannon Divergence) over time exhibits a rate transition.

C. Topological earth mover distance in the main experiment

The topological earth mover (TEM) distance [19], discussed in SI Sec. IV C, is the minimum number of topological (T1) transitions to transform one distribution of topological motifs to another distribution. While we mainly use the TEM distance to compute the structural order parameter $\langle d_{\text{hex}} \rangle$, this TEM distance can quantify topological distance between any pair of structures, beyond fixing one of them to be a perfect hexagonal crystal. This implies that, in addition to the KL divergence between topological landscapes, the TEM distance can also be used as a measure of dissimilarity between self-organized structures.

We first note that $\langle d_{\text{hex}} \rangle$ —equivalent to the TEM distance from each experimental snapshot and a perfect crystal—exhibits a transition at around 3.5 hours when the traveling state to fluctuating state transition occurs (Fig. S28a). Similarly, the pairwise distance map between experimental snapshots exhibits a bipartite pattern that separates structures before and after 3 hours (Fig. S28b).

Moreover, like in the topological flowscape, we can visualize the structural transition on coordinates of TEM distances from the initial and final structures (Fig. S28c). Interestingly, the sum of the two distances stay almost constant over the experiment. In addition, the self-organization progress, quantified as a diagonal displacement from initial to final states, exhibits a rate shift at the state transition as in other rate measures (Fig. S28d) (Secs. VII A-VII B).

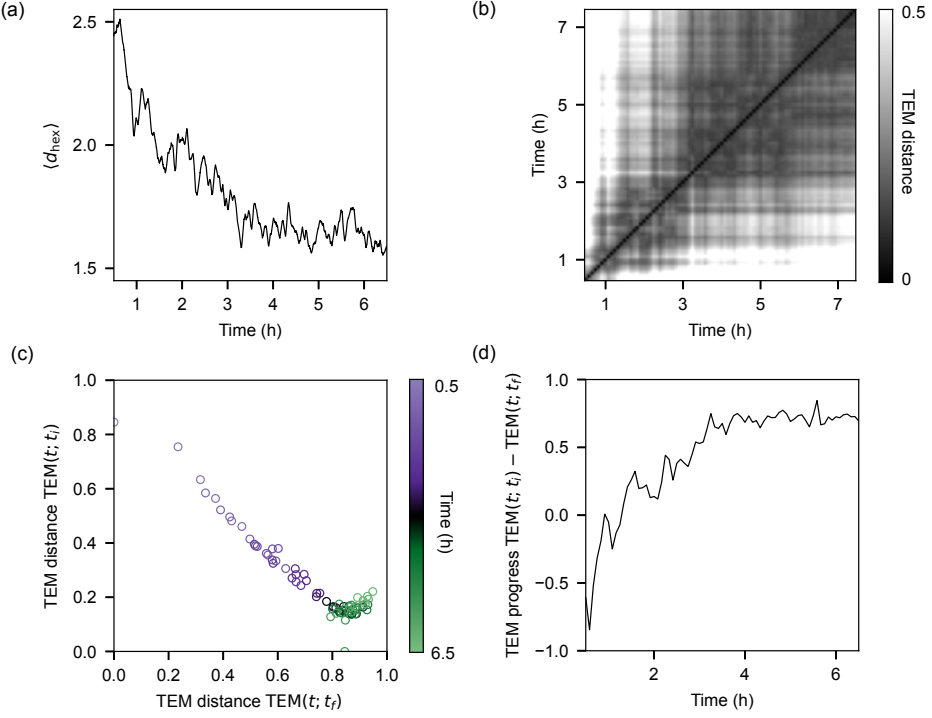


FIG. S28. **TEM distance provides an additional measure for dissimilarity between self-organized structures.** (a) Topological order parameter $\langle d_{\text{hex}} \rangle$ decreases over time. (b) Pairwise topological earth mover (TEM) distances between self-organized structures in the experiment at different times. The structure exhibits a bipartite block pattern between early time (before 3h) and late time (after 3h), which correspond to traveling and fluctuating states. (c) Topological flowscape using TEM distances from two reference states (the initial and final structures). (d) Diagonal displacement of TEM distances.

[1] C. Stringer, T. Wang, M. Michaelos, and M. Pachitariu, Cellpose: a generalist algorithm for cellular segmentation, *Nature Methods* **18**, 100 (2021).

[2] M. Pachitariu and C. Stringer, Cellpose 2.0: how to train your own model, *Nature Methods* **18**, 1634 (2022).

[3] D. B. Allan, T. Caswell, N. C. Keim, C. M. van der Wel, and R. W. Verweij, soft-matter/trackpy: v0.6.4 (2024).

[4] J. C. Crocker and D. G. Grier, Methods of digital video microscopy for colloidal studies, *Journal of Colloid and Interface Science* **179**, 298 (1996).

[5] T. H. Tan, A. Mietke, J. Li, Y. Chen, H. Higinbotham, P. J. Foster, S. Gokhale, J. Dunkel, and N. Fakhri, Odd dynamics of living chiral crystals, *Nature* **607**, 287 (2022).

[6] S. van der Walt, J. L. Schönberger, J. Nunez-Iglesias, F. Boulogne, J. D. Warner, N. Yager, E. Guillart, T. Yu, and the scikit-image contributors, Scikit-image: Image processing in python, *PeerJ* **2**, e453 (2014).

[7] S. R. Sternberg, Biomedical image processing, *Computer* **16**, 22 (1983).

[8] S. M. Pizer, E. P. Amburn, J. D. Austin, R. Cromartie, A. Geselowitz, T. Greer, B. ter Haar Romeny, J. B. Zimmerman, and K. Zuiderveld, Adaptive histogram equalization and its variations, *Computer Vision, Graphics, and Image Processing* **39**, 355 (1987).

[9] L. Breiman, Bagging predictors, *Machine Learning* **24**, 123 (1996).

[10] F. Pedregosa, G. Varoquaux, A. Gramfort, V. Michel, B. Thirion, O. Grisel, M. Blondel, P. Prettenhofer, R. Weiss, V. Dubourg, J. Vanderplas, A. Passos, D. Cournapeau, M. Brucher, M. Perrot, and E. Duchesnay, Scikit-learn: Machine learning in Python, *J. Mach. Learn. Res.* **12**, 2825 (2011).

[11] L. Breiman, J. Friedman, R. A. Olshen, and C. J. Stone, *Classification and Regression Trees* (Taylor & Francis, New York, NY, USA, 1984).

[12] E. H. Simpson, Measurement of diversity, *Nature* **163**, 10.1038/163688a0 (1949).

[13] C. J. Clopper and E. S. Pearson, On the use of confidence or fiducial limits illustrated in the case of the binomial, *Biometrika* **26**, 404 (1934).

[14] M. E. Tipping, Sparse Bayesian learning and the relevance vector machine, *J. Mach. Learn. Res.* **1**, 211 (2001).

[15] D. P. Wipf and B. D. Rao, Sparse Bayesian learning for basis selection, *IEEE Trans. Signal Process.* **52**, 2153 (2004).

[16] A. Krogh and J. Hertz, A Simple Weight Decay Can Improve Generalization, in *Advances in Neural Information Processing Systems*, Vol. 4, edited by J. Moody, S. Hanson, and R. Lippmann (Morgan-Kaufmann, Burlington, MA, 1991).

[17] D. J. MacKay, A practical Bayesian framework for backpropagation networks, *Neural Comput.* **4**, 448 (1992).

[18] D. J. MacKay, Bayesian interpolation, *Neural Comput.* **4**, 415 (1992).

[19] D. J. Skinner, B. Song, H. Jeckel, E. Jelli, K. Drescher, and J. Dunkel, Topological metric detects hidden order in disordered media, *Physical Review Letters* **126**, 048101 (2021).

[20] I. Borg and P. J. F. Groenen, *Modern multidimensional scaling: theory and applications*, 2nd ed., Springer Series in Statistics (Springer, New York, 2005).

[21] A. W. Bowman and A. Azzalini, *Applied smoothing techniques for data analysis: the kernel approach with S-Plus illustrations*, Vol. 18 (OUP Oxford, 1997).

[22] N. Shiraishi, K. Funo, and K. Saito, Speed limit for classical stochastic processes, *Physical Review Letters* **121**, 070601 (2018).

[23] T. Hatano and S.-i. Sasa, Steady-state thermodynamics of langevin systems, *Physical Review Letters* **86**, 3463 (2001).